

# UC San Diego

## UC San Diego Electronic Theses and Dissertations

### Title

Computational studies of the breathing motion of the metal -organic framework DMOF-1

### Permalink

<https://escholarship.org/uc/item/9325j2b7>

### Author

Grosch, Jason Scott

### Publication Date

2011

Peer reviewed|Thesis/dissertation

UNIVERSITY OF CALIFORNIA, SAN DIEGO

Computational Studies of the Breathing Motion of the Metal-Organic Framework  
DMOF-1

A thesis submitted in partial satisfaction of the  
requirements for the degree Master of Science

in

Chemistry

by

Jason Scott Grosch

Committee in Charge

Professor Francesco Paesani, Chair

Professor Seth Cohen

Professor John Weare

2011

Copyright

Jason Scott Grosch, 2011

All rights reserved.

The Thesis of Jason Scott Grosch is approved, is acceptable in quality and form for publication on microfilm and electronically:

---

---

---

Chair

University of California, San Diego  
2011

## DEDICATION

My thesis is dedicated to  
my family  
—Mom Roberta, Dad Kevin, and Brother Brian—  
my family-in-law  
—Mom Gul, Dad Abu, and Sister Tasneem—  
  
and my Wife,  
Jafreen Sadeque

## EPIGRAPH

To err is human — and to blame it on a computer is even more so.

*Robert Orben*

## TABLE OF CONTENTS

Signature Page .....	iii
Dedication .....	iv
Epigraph .....	v
Table of Contents .....	vi
List of Abbreviations .....	viii
List of Figures .....	ix
List of Tables .....	xi
Acknowledgements .....	xiii
Abstract of the Thesis .....	xiv
Chapter 1 Introduction .....	1
1.0 Outline .....	1
1.1 Historical Background of Metal-Organic Frameworks .....	1
1.2 Overcoming the Crystallization and Predictive Problems .....	2
1.3 Advantage of MOFs over Coordination Polymers .....	3
1.4 Nomenclature .....	4
1.5 Gas Separation .....	4
1.6 MOF Breathing .....	6
1.7 Hydrogen Storage .....	8
1.8 Computer Modeling .....	10
1.9 Purpose and Scope of Current Study .....	13
Chapter 2 DMOF-1 Background .....	15
2.1 Structure .....	15
2.1.2 Breathing Behavior .....	20
2.2 Experimental and Computational Background .....	20
2.2.1 Post-Synthetic Modification .....	22
Chapter 3 Methods .....	23
3.0 Introduction .....	23
3.1 Density Functional Theory .....	24
3.2 Møller-Plesset Perturbation Theory .....	26
3.3 Basis Sets .....	28
3.3.1 Basis Set Superposition Error .....	31
3.4 Partial Charge Determination .....	32
3.4.1 CHELP/CHELPG .....	33
3.5 Ab Initio Calculations .....	35
3.5.1 1,4-Benzenedicarboxylate .....	35
3.5.2 Post-Synthetically Modified BDC .....	37
3.5.3 DABCO .....	38
3.6 Molecular Dynamics .....	39
3.6.1 Non-Bonded Type Force Fields .....	42
3.6.1.1 Fully Non-Bonded Force Field .....	46
3.6.1.2 Restrained Force Field .....	51
3.6.2 Fully-Bonded Force Field .....	51

Chapter 4 Results and Discussion.....	57
4.1 Ab Initio Results.....	57
4.1.1 Post-Synthetic Modification.....	61
4.2 Non-Bonded Type Force Fields.....	62
4.2.1 Non-Bonded Force Field.....	62
4.2.2 Restrained Force Field.....	66
4.3 Fully-Bonded Type Force Field.....	68
Chapter 5: Conclusion .....	78
References.....	82



## LIST OF ABBREVIATIONS

BDC: 1,4-Benzenedicarboxylate

CGTO: Contracted Gaussian Type Orbital

CHELPG: CHarges from Electrostatic Potentials with Grid

DABCO: 1,4-diazabicyclo[2.2.2]octane

DFT: Density Functional Theory

DMOF-1+BEN: DMOF-1+benzene

DZ: Double Zeta

ECP: Effective Core Potential

GCMC: Grand Canonical Monte Carlo

GTO: Gaussian-Type Orbital

HF: Hartree-Fock

IPA: Isopropyl alcohol

LDA: Local Density Approximation

MIL: Materials Institute Lavoisier

MOF: Metal-Organic Framework

MP: Møller-Plesset

PGTO: Primitive Gaussian Type Orbital

SCF: Self-Consistent Field

STO: Slater-Type Orbital

## LIST OF FIGURES

Figure 1.1	Three of the most common two-connecting dicarboxylate ligands.....	3
Figure 1.2	One-step isotherm of adsorption that shows hysteresis on desorption.....	8
Figure 2.1	Structure of DMOF-1 with only one 1,4-dicarboxylate (BDC) and one axial 1,4-diazabicyclo[2.2.2]octane (DABCO) shown. Arrows indicating continuation of the lattice network .....	16
Figure 2.2	Available 4.8 Å x 3.2 Å window through the BDC grid ( <i>left</i> ) and 7.5 Å x 7.5 Å window down the axis of the DABCO ( <i>right</i> ).....	17
Figure 2.3	( <i>Top</i> ) Crystal structure of DMOF-1. The green and red axes represent the a and b unit cell lengths. ( <i>Bottom</i> ) Crystal structure of DMOF-1+2BEN .....	19
Figure 2.4	AM1 ( <i>left</i> ), AM2 ( <i>middle</i> ), and AM3 ( <i>right</i> ). Note that the methyl group capping the nitrogen is for illustration purposes only, and in reality it is connected to the DMOF-1 framework.....	22
Figure 3.1	The BDC-cluster to be optimized. The truncated Zn-clusters were capped with HCO <sub>2</sub> for charge neutrality. O = red, Zn = purple, C = grey, H = white .....	36
Figure 3.2	An illustration of the DABCO-cluster where the DABCO is bound to two Zn clusters.....	39
Figure 3.3	Unit cell of DMOF-1 showing the atomic labels .....	43
Figure 3.4	AM1-Cluster labels.....	49
Figure 3.5	Isolated AM4 illustrating labeling scheme .....	49
Figure 4.1	Harmonic fitting to Zn-O ( <i>left</i> ) and Zn-N ( <i>right</i> ) scans at the MP2 level of theory .....	60
Figure 4.2.	DMOF-1-AM1 intermediary configuration ( <i>top</i> ) and final configuration ( <i>bottom</i> ).....	65
Figure 4.3	Taking the unit cell axes along the direction of breathing is useful for comparison.....	69

Figure 4.4	DMOF-1+2BEN unit cell vectors during a 7.5 ns simulation. Statistics were outputted every 200 steps with a 1 fs time step. The correct unit cell parameters are marked with arrows .....72
Figure 4.5	Snapshots of the DMOF-1+2BEN simulation. Benzene in correct T-shape configuration (left) and parallel configuration (right) .....73

## LIST OF TABLES

Table 3.1A	Bonds used within the AMBER force field for the DMOF-1 framework.....	43
Table 3.1B	Angles used within the AMBER force field for the DMOF-1 framework.....	44
Table 3.1C	Dihedrals used within the AMBER force field for the DMOF-1 framework.....	45
Table 3.1D	Lennard-Jones parameters for the GAFF database atom types .....	46
Table 3.2	Two sets of partial charges used with DMOF-1 .....	47
Table 3.3A	Bonds used in the benzene force field.....	47
Table 3.3B	Angles used in the benzene force field.....	48
Table 3.3C	Dihedrals used in the benzene force field.....	48
Table 3.4	Partial charges on atoms of BDC-AM1-cluster.....	50
Table 3.5	Atomic charges of the AM2 to AM4 alkyl chains. Charges on atoms not present in an amine group are labeled with n/a.....	50
Table 3.6A	Bond parameters for the fully-bonded force field .....	52
Table 3.6B	Angle parameters for the fully-bonded force field .....	53
Table 3.6C	Dihedral parameters for the fully-bonded force field.....	54
Table 3.7A	Bonds for the IPA force field.....	55
Table 3.7B	Angles for the IPA force field .....	56
Table 3.7C	Dihedrals for the IPA force field .....	56
Table 3.7D	Lennard-Jones parameters for the IPA force field.....	56
Table 4.1	BDC ligand charges from different ab initio methods.....	58
Table 4.2	DABCO ligand charges from different ab initio methods. Isolated DABCO ligands do not have Zn-N distances, which are labeled n/a.....	58

Table 4.3	BDC–cluster optimizations with different ab initio methods and basis sets. Use of the LAN2DZ ECP basis set is indicated next to the functional where appropriate .....	59
Table 4.4	Comparison between original M062X charges and the BDC-cluster using MP2-theory with LAN2DZ basis set charges with Zn radius at 1.1 Å and 1.4 Å The length of axes are in Å .....	63
Table 4.5	Percent error of simulated DMOF-1 Zn–distances relative to crystal data .....	63
Table 4.6	Results of DMOF-1 and DMOF-1 with varying amounts of benzene and IPA per unit cell. For systems with no experimental data the percent Error is listed as n/a. The length of axes are in Å .....	70
Table 4.7	DMOF-1-AM1 to DMOF-1-AM4 unit cell vectors. The length of axes are in Å .....	76

## ACKNOWLEDGEMENTS

I would like to acknowledge Professor Francesco Paesani for his support as the chair of my committee and mentor in both science and life. Without his constancy, love for science, and wisdom I would never have finished my thesis nor my time at UCSD. Few people would have been willing to work past my considerable character flaws. I am blessed to have Francesco as a role model. Thank you.

I would like to acknowledge the people I have worked with in my lab: Wei Lin, Greg Medders, Nico Sawaya, Duo Song, Jeffrey Sung, Kyoyeong Park, Pilar Montellano, and Alan Chan. It was a pleasure to have their support and friendship.

I would like to acknowledge Eyad Alnaslah. Assalamu alaikum wa rahmatullahi wa barakatuhu, my friend.

Most of all, I would like to acknowledge my wife Jafreen for her thorough and tireless editing of my thesis.

## ABSTRACT OF THE THESIS

Computational Studies of the Breathing Motion of the Metal-Organic Framework  
DMOF-1

by

Jason Scott Grosch

Master of Science in Chemistry

University of California, San Diego, 2011

Professor Francesco Paesani, Chair

The breathing behavior of metal-organic frameworks (MOFs) is an exciting new phenomenon in which a framework significantly changes unit cell shape depending on adsorbent, change in pressure, or temperature. There are few force fields capable of computationally describing MOF breathing behavior, and they exist only for MIL-53. In this study, fully flexible force fields were created for the MOF “DMOF-1” ( $\text{Zn}_2(\text{BDC})_2(\text{DABCO})$ ), which is known to breathe with the addition of benzene and isopropyl alcohol, and upon post-synthetic modification with amines. Over the course

of the study, three flexible force fields were examined: a non-bonded force field, a restrained force field, and a fully-bonded force field.

The non-bonded and restrained force fields represented the Zn–ligand bonds by electrostatic interactions, and did not reasonably simulate the DMOF-1 breathing behavior. The fully-bonded force field explicitly described the Zn–ligand interactions and was found to quantitatively reproduce experimental data of DMOF-1 and of DMOF-1 with benzene, and qualitatively reproduce DMOF-1 with isopropyl alcohol. The aminated DMOF-1 series DMOF-1-AM1 to DMOF-1-AM4 was not as successfully modeled, however. The fully-bonded force field incorrectly predicted the DMOF-1-AM1 and DMOF-1-AM2 structures to be in a large pore configuration. This highlights a potential issue with force field transferability between different breathing systems for DMOF-1, a current problem with flexible MOF force fields. At present, it is not clear whether the difficulties in transferability to the aminated framework are due to insufficient representation of the amine chains or a more fundamental problem describing the framework flexibility.



# Chapter 1

## Introduction

### 1.0 Outline

This section introduces metal-organic frameworks (MOFs) in the context of highly porous materials such as zeolites. Their historical synthesis, applications in gas storage and separation, and unique “breathing” motion are discussed.

### 1.1 Historical Background of Metal-Organic Frameworks

Highly porous materials such as amorphous activated alumina and rigid periodic zeolites have long been employed in industrial applications for gas purification, separation, and catalysis. Within the last 20 years, a host of periodic solid materials such as metal-organic frameworks (MOFs), covalent-organic frameworks (COFs), and zeolitic-imidazole frameworks (ZIFs) have emerged as new porous solids. Rigid, porous, and periodic, these novel solids are similar to their purely inorganic zeolitic counterparts. Of these exciting new materials, the most research has been conducted on MOFs, which are metal ion clusters, generally transition metal ions, linked together by rigid organic ligands in a periodic lattice of directional covalent bonds.

## 1.2 Overcoming the Crystallization and Predictive Problems.

MOFs were originally thought to be a synthetic impossibility because of the difficulty of making a three-dimensional periodic structure from directional covalent bonds, known as the crystallization problem.<sup>1</sup> In addition, if a three-dimensional periodic structure were to be synthesized, there would be no way to predict the resulting structure. This was clearly stated by John Maddox, “One of the continuing scandals in physical sciences is that it remains in general impossible to predict the structure of even the simplest crystallographic solids from knowledge of their chemical composition.”<sup>1,2</sup> Despite these obstacles, in 1998 Yaghi et al. synthesized the first stable MOF, which they named “MOF-2”.<sup>3,4</sup> MOFs have overcome the crystallization problem in part because the counter-ions for the metal clusters are the connecting organic ligands. This allows for general stability upon solvent evacuation.

The problem of predicting MOF structures has been overcome by viewing MOF precursors as geometric building blocks such as “node and spacers”, and “secondary building units”, which are often stable metal clusters bound to carboxylates acting as joints.<sup>5</sup> By knowing the reaction that creates the secondary building unit, the overall topology can be predicted because the reacting organic linker remains intact. These specific features allow chemists to predict MOFs from their constituent components. For example,  $Zn_4O(O_2C-)_6$  forms an octahedral joint where the  $O_2C-$  groups act as points of extension that form the well-known MOF-5 of unit cell  $Zn_4O(BDC)_3$  when reacted with 1,4-benzenedicarboxylate (BDC).<sup>6</sup> The BDC connects two metal clusters and can be replaced with similar “two-connecting” ligands such as 1,4-

naphthalenedicarboxylate and biphenyl-4,4'-dicarboxylate to maintain the same overall connectivity but varying pore size. Figure 1.1 shows three common two-connecting ligands.

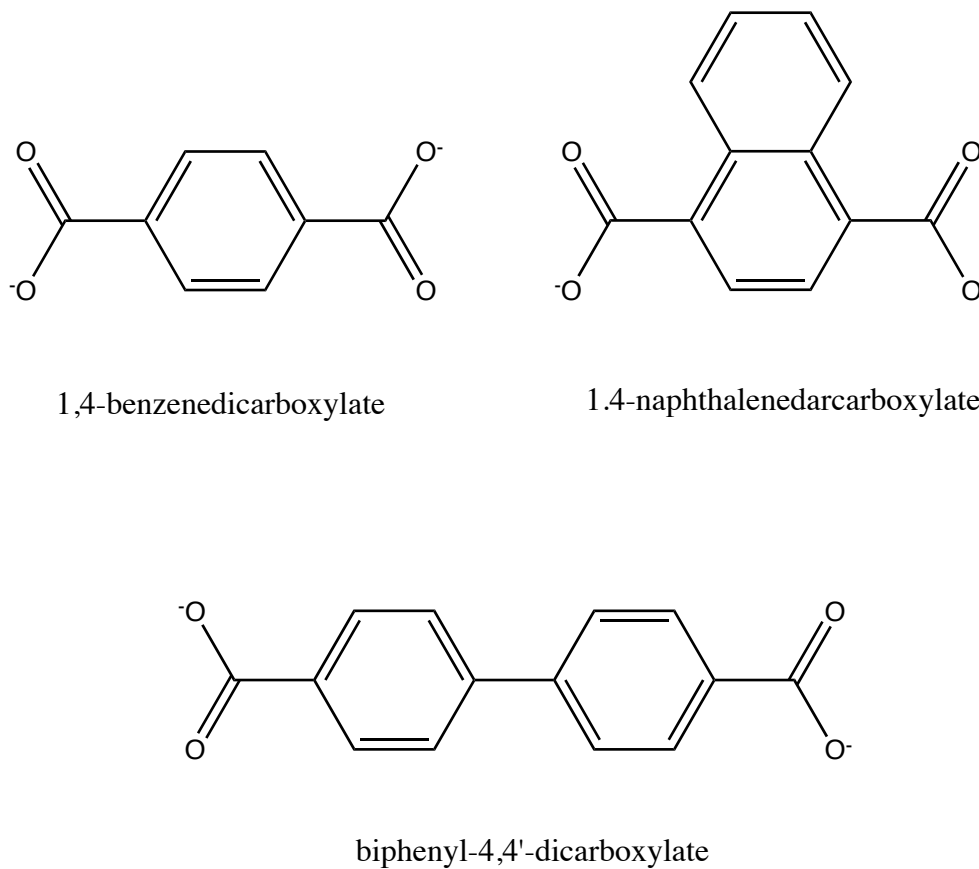


Figure 1.1. Three of the most common two-connecting dicarboxylate ligands.

### 1.3 Advantage of MOFs over Coordination Polymers

MOFs and coordination polymers (CPs) are often considered synonymous, although there are several distinguishing features. MOF maintain stability after solvent

evacuation, a major advantage over traditional CPs, which usually have counter-ions in the solvent making them unstable upon solvent removal. Moreover, the bond valences between ligands and metals in MOFs are usually higher and stronger than in CPs,<sup>6</sup> and MOFs have several metal atoms per node while CPs usually consist of a single metal atom.<sup>6</sup>

#### **1.4 Nomenclature**

It is important to note that although the name “metal-organic framework” is most commonly used, other names include “porous coordination polymer” and “porous coordination network”. Frequently, new MOFs are given a prefix that represents the university where the compound was created, such as “MIL” for Materials Institute Lavoisier and “HKUST” for Hong Kong University of Science and Technology. Yaghi et al. recently developed nomenclature parallel to the concept of nets that describes crystal structures and CPs, available online at Reticular Chemistry Structure Database.<sup>6</sup> Despite efforts to standardize MOF nomenclature, currently no one system has been agreed upon.

#### **1.5 Gas Separation**

The relative ease of synthesizing new MOFs by using similarly connecting organic ligands and metals allows for their systematic investigation while maintaining unchanged topology. MOFs elicit unprecedentedly large surface areas that result from

stable evacuated frameworks with large pore sizes. With the maximum recorded Langmuir surface area of 10,400 m<sup>2</sup>/g, MOFs have the highest recorded surface area of any porous material, which naturally allows effective surface adsorption.<sup>7</sup> Significant experimental and computational efforts have explored the physicochemical properties of MOFs by characterizing the effects of pore size, framework composition, uncoordinated metal sites, and framework flexibility. In order to design materials for effective application in gas separation and purification, CO<sub>2</sub> capture, and hydrogen fuel storage, it is particularly important to understand how MOFs adsorb different types of gases.

In porous materials, gas separation occurs in four major ways: molecular sieving by size and shape exclusion, preferential framework adsorbent interactions (i.e., the thermodynamic equilibrium effect), different diffusion rates into pores, and the quantum sieving effect for small molecules.<sup>8</sup> In molecular sieving, steric hindrance between the MOF pore size and kinetic diameter of a molecule excludes molecules due to size effects. For example, this size-induced selective adsorption of H<sub>2</sub> over N<sub>2</sub> has been shown at 77K in several MOFs: Mg<sub>3</sub>(ndc)<sub>3</sub> (ndc = 2,6-naphthalenedicarboxylate),<sup>9</sup> Sm<sub>4</sub>Co<sub>3</sub>(pyta)<sub>6</sub>(H<sub>2</sub>O)<sub>x</sub> (pyta = 2,4,6-pyridinetricarboxylic acid),<sup>10</sup> Cu(F-pymo)<sub>2</sub> (F-pymo = 5-fluoropyrimidin-2-olate),<sup>11</sup> and Zn<sub>2</sub>(cnc)<sub>2</sub>(dpt)·Guest (cnc = 4-carboxycinnamic and dpt = 3,6-di-4-pyridyl-1,2,4,5-tetrazine).<sup>12</sup> Similarly, Zn<sub>2</sub>(cnc)<sub>2</sub>(dpt) selectively adsorbs CO<sub>2</sub> over CH<sub>4</sub> based on size and shape exclusion.<sup>8</sup> Preferential adsorption occurs through adsorbate-surface interactions such as hydrogen bonding, polarity, and quadrupole moments. Preferential adsorption of C<sub>2</sub>H<sub>2</sub> over CO<sub>2</sub> was accomplished in the MOF Cu<sub>2</sub>(pzdc)<sub>2</sub>(pyz) (pzdc = pyrazine-2,3-dicarboxylate and pyz = pyrazine),<sup>13</sup>

presumably through effective van der Waals framework-sorbent interactions. It is important to note that it is difficult to perform the same separation using conventional zeolites and activated carbons because  $C_2H_2$  and  $CO_2$  have similar dynamic radii. Other studies have shown that  $Zn_2(bptc)$  ( $bptc = 2,2',3,3'$ -benzophenonetetracarboxylate) preferentially adsorbs  $CHCl_3$ ,  $CH_3OH$ , and  $H_2O$  over hexane and pentane because of the establishment of hydrogen bonding networks.<sup>14</sup> Also,  $Zn_2(bptc)$  selectively separates benzene and toluene from hexane and pentane through  $\pi$ - $\pi$  interactions.<sup>9</sup>

## 1.6 MOF Breathing

The sorption capabilities in some MOFs are enhanced by their flexibility. Some MOFs exhibit “breathing”,<sup>15,16,15,16,15,16,15,16,17</sup> which is the reversible transformation of one unit cell shape into another by external stimuli such as gas adsorption or change in pressure and temperature.<sup>18,19</sup> The breathing motion can be understood in general terms by considering the presence of labile “weak spots” between the metal centers and the ligands.<sup>16</sup> In combination with proper geometry, the breathing allows for dramatic changes in atomic positions. In some MOFs a change of 8 Å in the unit cell vectors has been observed without any breaking of the chemical bonds.<sup>16</sup>

The most well-known MOF that “breathes” is MIL-53 ( $Al_2OH(BDC)_2$ ), whose framework contracts from a large pore (LP) structure into a narrow pore (NP) structure upon addition of water. This motion is induced by the formation of hydrogen bonds between the water molecules and the MIL-53 hydroxyl group. Whereas zinc-based MOFs such as MOF-5 ( $Zn_4O(BDC)_3$ ) dissolve readily in water, the MIL-53 is uniquely

hydrostable as a result of the  $3^+$  metal ion charges.<sup>17,18</sup> MIL-53 selectively adsorbs  $\text{CO}_2$  over  $\text{CH}_4$  due to quadrupole interactions between its framework and adsorbates. Interestingly,  $\text{CO}_2$  also induces a change in the framework from LP to NP. At higher  $\text{CO}_2$  pressures MIL-53 again opens into the LP structure, resulting in additional volume that leads to a distinct step in the isotherm of adsorption.<sup>8,19</sup>

The breathing motion due to adsorption gives MOFs additional capabilities of selectively sieving gases as their pore sizes change in the presence of specific adsorbates. Breathing can be used to selectively filter gases by opening MOF pores at specific pressures.  $\text{Cu}(\text{dhbc})_2(4,4'\text{-bpy})$ <sup>9,20</sup> (dhbc = 2,5-dihydroxybenzoic acid and 4,4'-bpy = 4,4'-bipyridine) in its hydrated form, this MOF has been shown to selectively adsorb  $\text{CO}_2$ ,  $\text{CH}_4$ ,  $\text{O}_2$ , and  $\text{N}_2$  at various high pressures while effectively having zero adsorption at low pressures. The breathing motion results in noticeable steps in the isotherms of adsorption and desorption, which leads to hysteresis. Figure 1.2 illustrates a one-step isotherm of adsorption with hysteresis on desorption. This is the result of a collective framework motion that snaps open and close taking up and pushing out adsorbent molecules.

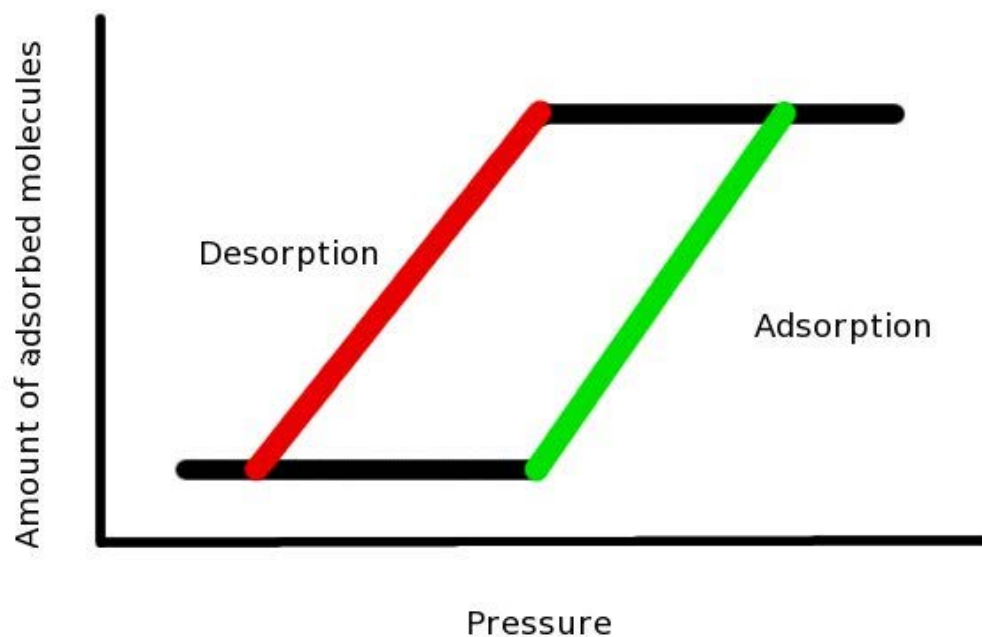


Figure 1.2. One-step isotherm of adsorption that shows hysteresis on desorption.

## 1.7 Hydrogen Storage

Hydrogen storage in MOFs is an active area of experimental and theoretical research.<sup>21</sup> Hydrogen is a promising alternative energy source to fossil fuels and can significantly lower carbon emissions. Despite having exceptional energy density, hydrogen is very volatile and difficult to store at ambient temperature and pressure.<sup>22</sup> The high surface areas of MOFs make for a potentially viable alternative to the well-studied, heavier metal hydrides for hydrogen storage.<sup>23</sup> Ideally MOFs should breathe as a result of hydrogen adsorption to take advantage of the hysteresis, which allows for a large amount of hydrogen fuel to be quickly desorbed. Hydrogen usually adsorbs onto



MOF surfaces through weak van der Waals interactions, a process called “physisorption”, which directly correlates with the available surface area.

Several methods are being explored to improve the weak enthalpy of adsorption of hydrogen, typically 4 to 7 kJ mol<sup>-1</sup>, to a more desired enthalpy of 20 kJ mol<sup>-1</sup> through increasing the density of open metal sites, catenation, and spillover.<sup>21</sup> Care must be taken to avoid H<sub>2</sub>-metal bonds that can reach 80-90 kJ mol<sup>-1</sup>, too strong of an interaction for a controlled release in fuel cells.<sup>21</sup> A more controlled release could occur with Li<sup>+</sup> ions, which have a binding energy of 27 kJ mol<sup>-1</sup> with gas phase hydrogen. However, the Li<sup>+</sup>-hydrogen interaction is significantly lessened within MOF structures due to charge quenching.<sup>21</sup> The Li<sup>+</sup> hydrogen charge quenching is clearly demonstrated by Li<sub>2</sub>Zn<sub>3</sub>[Fe(CN)<sub>6</sub>]<sub>2</sub>·2H<sub>2</sub>O, which has a H<sub>2</sub> heat of adsorption of 7.9 kJ mol<sup>-1</sup>.<sup>24</sup>

MOFs with the largest pores and surface areas are ill-suited for hydrogen storage because of the weak hydrogen-framework interactions. The preferential positions for hydrogen adsorption are open metal sites and entrances to small pores, where the molecules framework interactions is greatest.<sup>21</sup> Thus, an efficient material for hydrogen storage must contain a large volume of small spaces. One method to reduce the amount of large spaces in a framework is through interpenetration/catenation that directly embeds several frameworks into each other. Controlling the interpenetration is a difficult synthetic challenge and only one MOF in existence, Cu<sub>3</sub>(tatb)<sub>2</sub> (tatb = 4,4',4''-s-triazine-2,4,6-triyltribenzoate),<sup>25</sup> has synthetically controlled catenated and non-catenated forms. Its catenated form adsorbs 1.9 wt% H<sub>2</sub> at 1 bar and 77 K, 0.6 wt% more than the non-catenated form. Although catenated frameworks increase the heat of adsorption, it is believed that the increase of the heat of adsorption does not compensate

for the decrease in pore volume and ultimately decreases the total loading of hydrogen in many MOFs.

## 1.8 Computer Modeling

Computer models have been used to simulate MOF framework-adsorbent interactions using empirical force fields that effectively describe the energetics of both bonded and non-bonded interactions. The bonded terms of an empirical force field describe the bonds, angles, and dihedrals, and the non-bonded interactions describe the electrostatic and van der Waals forces. The non-bonded interactions are usually described by non-polarizable point charges on each atom to describe the coulombic interactions, and Lennard-Jones potentials for each atom pair to describe repulsion and dispersion interactions. The interactions within a simulation of finite number of atoms do not accurately represent a real chemical system. Thus, periodic boundary conditions are applied to account for the exposed surfaces in a simulation with a finite number of atoms. The periodic boundaries give an infinite distance for non-bonded forces to interact, so a real space cutoff is applied to both the van der Waals and coulombic interactions, after which the Ewald summation technique is used to account for long-range periodicity.<sup>26</sup> Common force field parameters are taken from the DREIDING,<sup>27</sup> CHARMM,<sup>28</sup> and UFF<sup>29</sup> force fields.

After a force field is chosen to represent the MOF framework, isotherms of adsorption can be calculated by the grand canonical Monte Carlo (GCMC) method.<sup>30</sup> This technique involves holding the chemical potential, volume, and temperature

constant throughout the simulation while allowing the number of molecules to fluctuate until equilibrium is reached. The chemical potential is directly related to the pressure by an equation of state, which allows the entire isotherm to be calculated.<sup>30</sup> Each step in the GCMC simulation involves a random insertion or deletion, translation, or rotation of adsorbent molecules. The insertion and deletion steps are based on Boltzmann-type weighting. During the simulation, the framework is generally held fixed in its crystallographic structure, which provides the significant advantage of not needing to describe the bonded framework interactions, a time-consuming process.

Computational modeling of MOF isotherms of adsorption using GCMC simulations with TraPPE<sup>31</sup> force field parameters for the adsorbate molecules generally reproduce experimental values. Previous studies demonstrate that GCMC simulations can also significantly overestimate the experimental values.<sup>32</sup> In this regard, it is important to note that the experimentally derived crystal quality directly impacts the isotherms of adsorption. Structural impurities such as partial framework collapse and incomplete solvent removal reduce the amount of gas that can be adsorbed, whereas in computer simulations the structure always corresponds to a perfectly aligned evacuated lattice. Because of this, simulations have larger volumes that overestimate total number of adsorbed molecules at high pressure. Also, the simulations tend to incorrectly model the number of adsorbed molecules at low pressures, where the adsorbate-framework interactions are less influenced by volume effects.

Though GCMC simulations are usually successful at reproducing experimental isotherms of adsorption, this is not the case for breathing MOFs, which are failed to be correctly reproduced. Traditional GCMC simulations that use rigid frameworks directly

conflict with the necessary flexibility required to produce breathing. Attempts have been made to circumvent the rigid framework with hybrid GCMC and molecular dynamics simulations, GCMC/MD, where after a GCMC step molecular dynamics (MD) equilibrates the framework and gas molecules. Unfortunately, this method failed to reproduce the NP to LP transition in MIL-53 with CO<sub>2</sub>.<sup>33</sup>

Currently, force fields and ab initio methods such as density functional theory (DFT) also fail to quantitatively describe the expansion and contraction of MOFs caused by thermal fluctuations and external stress. Young's modulus is a measure of the stiffness along an axial loading, which is defined as the ratio of lateral strain to axial strain. The experimental value of Young's modulus for MOF-5 along the (100) direction is  $2.7 \pm 1.0$  GPa, while force fields and DFT predict 35.5 GPa and 21.6 GPa, respectively.<sup>34</sup>

The inability of force fields to correctly describe the expansion and contraction of MOFs does not pose an issue for modeling the breathing behavior using MD. MIL-53 is the only MOF that has been modeled successfully with CO<sub>2</sub>, H<sub>2</sub>O, and H<sub>2</sub>S.<sup>35-39</sup> These simulations were able to reproduce experimental values but required separate force fields for each simulation. Férey et al. indicated that twisting of the BDC ligands along the Zn–O–C–C dihedral is the primary cause for the LP/NP transition in MIL-53.<sup>41,42</sup> Fully-bonded force fields, which explicitly account for Zn–ligand interactions were necessary to describe the flexibility of MIL-53. In contrast, force fields based entirely on non-bonded interactions that describe molecular bonding in terms of coulombic forces were too flexible.

DMOF-1,<sup>40</sup> also known as Zn MOF, with unit cell formula  $Zn_2(BDC)_2(DABCO)^{41}$  (DABCO = 1,4-diazabicyclo[2.2.2]octane), breathes upon adsorption of both benzene and isopropyl alcohol (IPA), contracting from a LP to NP state. Unlike MIL-53 that breathes because of a strongly interacting hydroxyl group, DMOF-1 does not contain any strongly interacting framework moieties. In the DMOF-1 framework, post-synthetic modification of BDC ligands with amine chains of different lengths also directly affects the breathing behavior.<sup>40</sup> This study will focus on the computational modeling of DMOF-1 flexibility, an investigation not previously conducted.

## 1.9 Purpose and Scope of Current Study

The purpose of this study is to create the first fully flexible force field capable of describing the framework flexibility of DMOF-1 using MD. Rigid framework force fields that are often used to model gas sorption in MOFs are not suitable for observing MOF breathing. The flexible force field is validated by reproducing both the parameters of the evacuated, LP unit cell and the parameters of the contracted, NP unit cell with benzene. Simulating DMOF-1 with IPA provides a strict test for the transferability of this force field to systems other than benzene adsorption. It is anticipated that if the experimentally determined NP structure is qualitatively obtained following addition of IPA, then the force field is generally transferable. The newly developed force field is used to simulate DMOF-1 with post-synthetically modified BDC ligands with amines, which have been shown to affect the framework flexibility.<sup>40</sup>

These simulations will help identify the molecular interactions responsible for the observed, and not understood, MOF breathing.

Partial charges for the force field are obtained from Møller-Plesset perturbation theory and DFT calculations performed with the Gaussian 09<sup>42</sup> quantum chemistry package. The force field parameters for bonds, angles, dihedrals, and van der Waals forces (modeled by Lennard-Jones parameters) are obtained from the GAFF<sup>43,44</sup> database available in the AMBER MD package. In this study the effectiveness of fully-bonded and non-bonded force fields on modeling the properties of DMOF-1 with and without benzene are compared. The effects on force field accuracy using partial charges derived for the BDC and DABCO ligands in isolation and in the presence of Zn clusters are also investigated. The MD simulations are conducted using both AMBER 11<sup>45</sup> and DL\_POLY\_4<sup>46</sup> MD packages.

## Chapter 2

### DMOF-1 Background

#### 2.1 Structure

Solvated DMOF-1 was originally synthesized by Kim et al. in 2004 by heating  $\text{Zn}(\text{NO}_3)_2$ , terephthalic acid, and DABCO in a solution of dimethylformamide (DMF) for two days at 110 °C to yield a crystalline solid of formula  $\text{Zn}_2(\text{BDC})_2(\text{DABCO}) \cdot 4\text{DMF} \cdot \frac{1}{2}\text{H}_2\text{O}$ .<sup>47</sup> The BDC ligands flex outward in the solvated crystal structure and straighten upon solvent evacuation to yield a large pore (LP) ordered tetragonal unit cell consisting of repeating networks of  $\text{Zn}_2(\text{BDC})_2(\text{DABCO})$ , or “DMOF-1”.

The BDC ligands form two-dimensional grids with  $\text{Zn}_2$  paddle-wheel clusters. The formed BDC layers are stacked on each other, tethered by DABCO ligands through weak N–Zn bonds. Each Zn atom forms four Zn–O bonds, one BDC per bond, and a Zn–N bond. Figure 2.1 shows a three-dimensional depiction of DMOF-1. The Zn clusters correspond to classical paddle-wheel  $\text{Zn}_2(\text{O}_2\text{C})_4$  secondary building units. Similar to many MOFs, DMOF-1 has a large Brunauer, Emmett, and Teller surface area of  $1450 \text{ m}^2\text{g}^{-1}$ .<sup>47</sup> The unit cell volume is  $1147.6 \text{ \AA}^3$  with 61.3%<sup>48</sup> available to adsorbents. The scaffold-like structure leaves open pores of  $4.8 \text{ \AA} \times 3.2 \text{ \AA}$  along the

BDC grid ( $a$  and  $b$  axes), and  $7.5 \text{ \AA} \times 7.5 \text{ \AA}$  along the axis of the DABCO, ( $c$  axis).<sup>49</sup>

Figure 2.2 illustrates the two different windows.

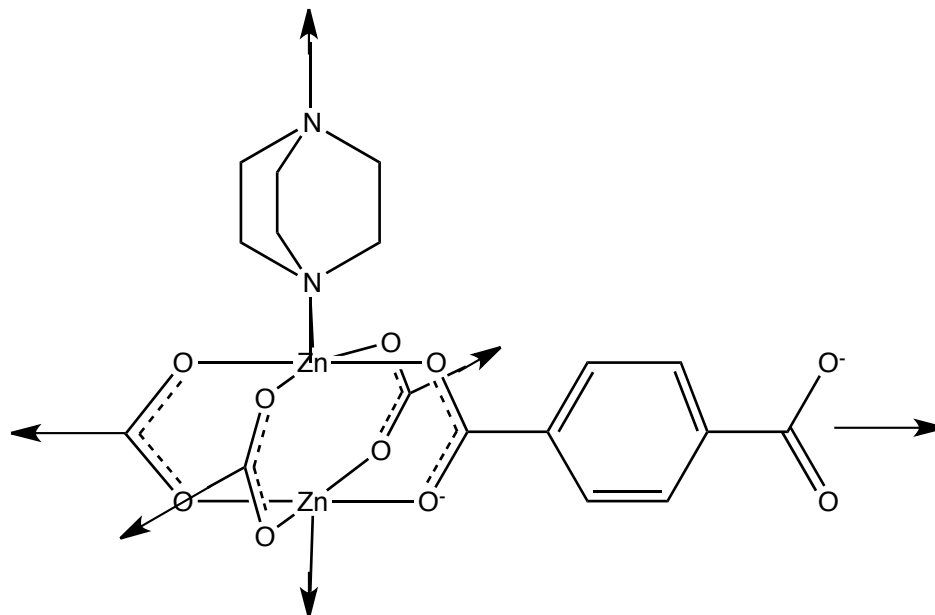


*Figure 2.1.* Structure of DMOF-1 with only one 1,4-dicarboxylate (BDC) and one axial 1,4-diazabicyclo[2.2.2]octane (DABCO) shown. Arrows indicating continuation of the lattice network.



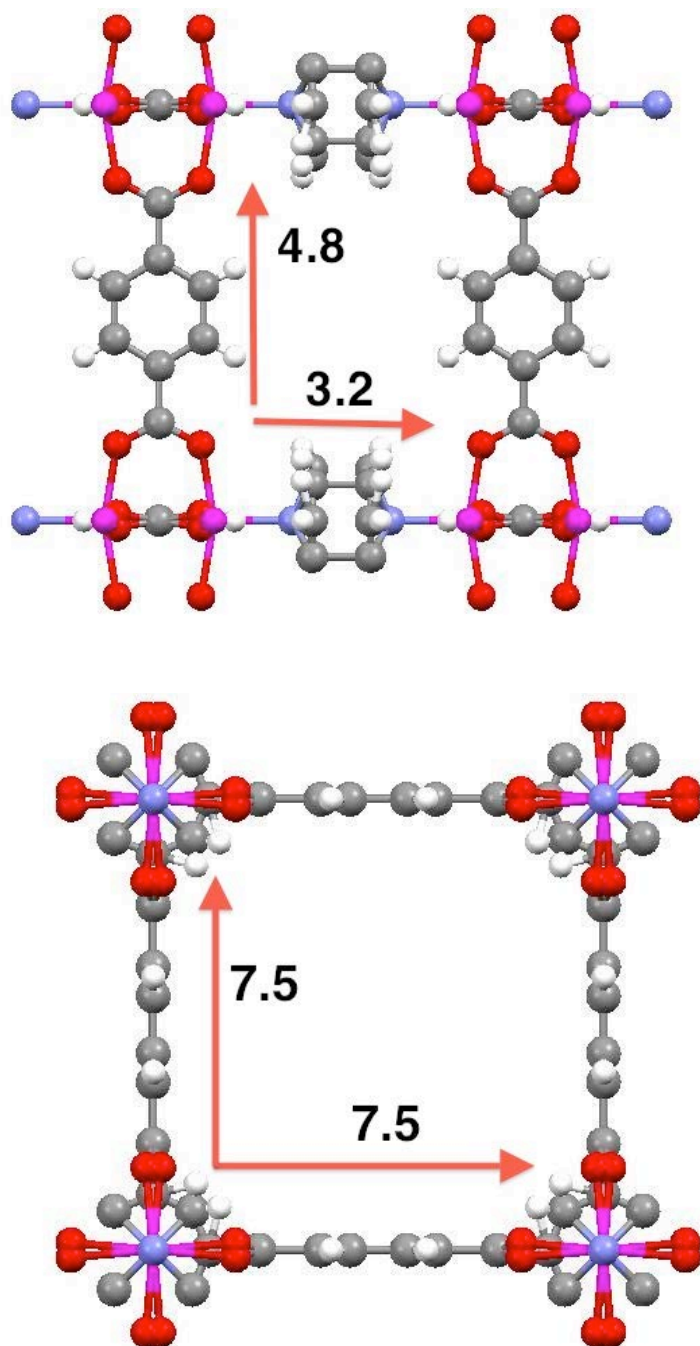
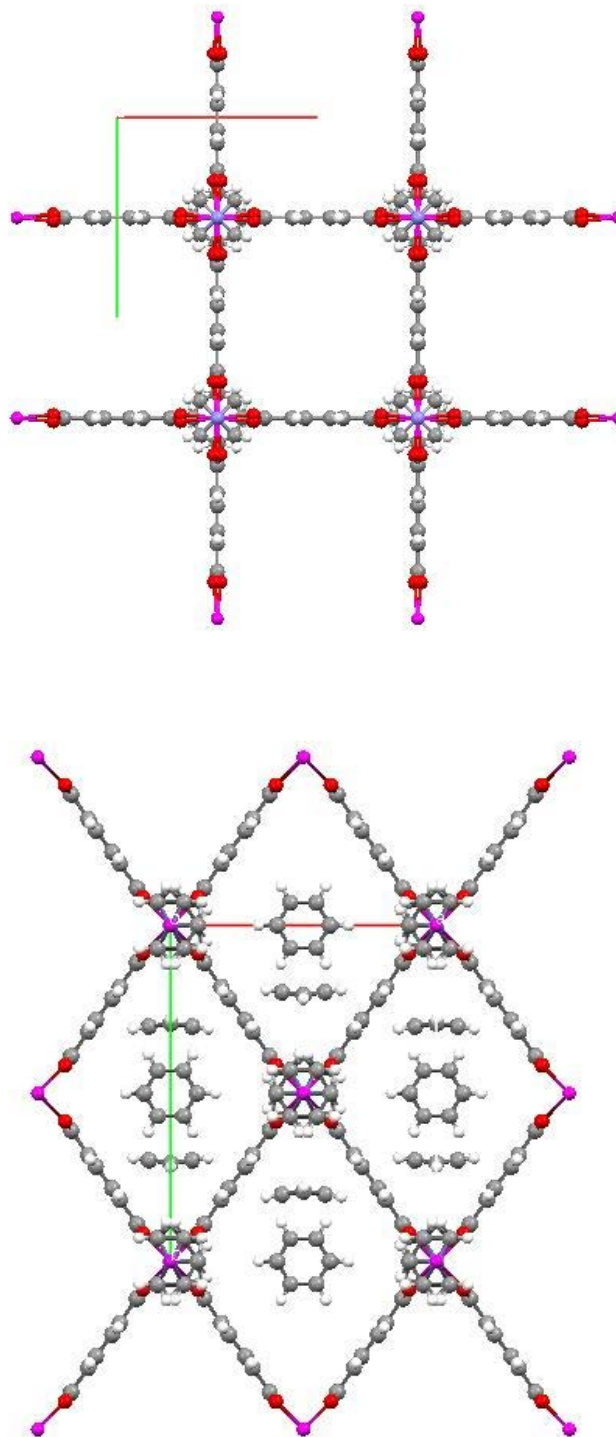


Figure 2.2. Available 4.8 Å x 3.2 Å window through the BDC grid (*top*) and 7.5 Å x 7.5 Å window down the axis of the DABCO (*bottom*). Blue = N, pink = Zn, white = H, grey = C. Coordinates obtained from crystal information.

DMOF-1 is the second known MOF to exhibit breathing behavior, the first being MIL-53(Al). Often, the change in unit cell vectors after breathing must be inferred by X-ray powder diffraction (PXRD). DMOF-1, however, is highly unique in that it maintains crystallinity after both solvent exchange with benzene and desolvation and can be studied through single crystal X-ray diffraction. The adsorption of benzene yields  $\text{Zn}_2(\text{BDC})_2(\text{DABCO}) \cdot 2\text{C}_6\text{H}_6$ , hereafter referred to as “DMOF-1+2BEN,” which contracts into a narrow pore (NP) orthorhombic unit cell. Figure 2.3 compares the LP DMOF-1 with the NP DMOF-1+2BEN. Kim et al. exchanged the BDC and DABCO ligands with other two-connecting carboxylates and nitrogen-containing ligands, and found the resulting structure maintained crystallinity and overall topology.<sup>50</sup>



*Figure 2.3 (Top)* Crystal structure of DMOF-1. The green and red axes represent the a and b unit cell lengths. The unit cell parameters are  $a = b = 10.9288 \text{ \AA}$ ,  $c = 9.6084 \text{ \AA}$ . *(Bottom)* Crystal structure of DMOF-1+2BEN. The unit cell parameters are  $a = 17.0664 \text{ \AA}$  (green),  $b = 13.5004 \text{ \AA}$  (orange),  $c = 9.6715 \text{ \AA}$ .

### 2.1.2 Breathing Behavior

In 2007, Uemura et al. found that isopropyl alcohol (IPA) elicits breathing behavior in DMOF-1, giving the characteristic adsorption/desorption hysteresis in the isotherm of adsorption.<sup>51</sup> Unlike benzene adsorption, the IPA-induced LP to NP transition does not preserve material crystallinity and was thus characterized by PXRD.<sup>51</sup> The isotherms indicate that 3 IPA molecules per unit cell induce a structural contraction from LP to NP with loss of crystallinity. The framework then expands back into the LP structure in the presence of 4.5 IPA per unit cell and regains its crystallinity, which was characterized by single crystal data. The crystal data indicate that the LP structure is maintained by IPA dimers hydrogen bonding through the windows formed by the BDC grid.

## 2.2 Experimental and Computational Background

Using experimental and computational methods, several groups have studied the gas sorption properties of DMOF-1.<sup>49,52</sup> DMOF-1 has been shown to preferentially adsorb CO<sub>2</sub> over other adsorbents such as N<sub>2</sub>, H<sub>2</sub>, and methane.<sup>41,53</sup> However, like other Zn-based MOFs, DMOF-1 is unstable in water and irreversibly dissolves in aqueous solutions.<sup>54</sup> DMOF-1 has also been shown to reversibly displace the DABCO ligands under mildly humid conditions while maintaining crystallinity.<sup>55</sup> Chaffee et al. studied

CO<sub>2</sub> gas sorption properties and water tolerance to find that the structure irreversibly decomposes at 60% humidity.<sup>56</sup>

Snurr et al. computationally investigated the sorption capacity of several alkanes in DMOF-1 via the GCMC method.<sup>57</sup> Other groups have combined experimental and computational methods to study the gas sorption properties. Johnson et al. studied the H<sub>2</sub> experimental adsorption isotherms at 77 K and 298 K and compared them to computational adsorption isotherms calculated using the from the UFF and DREIDING force fields.<sup>32</sup> The Feynman-Hibbs effective potential was used to account for quantum effects at low temperatures.<sup>58,59</sup> Johnson et al. found that results calculated with the DREIDING force field parameters agree with experimental data at low pressures but underestimate the amounts of H<sub>2</sub> at high pressures. The results obtained with the UFF force field significantly overestimate the amount of H<sub>2</sub> at low pressures while slightly overestimating the amount of H<sub>2</sub> at high pressures. At room temperature the result obtained with the DREIDING force field agree well with the experimental data while the result obtained with the UFF force field overestimate the H<sub>2</sub> loading at all pressures.

Similarly, Walton and Karra compared the experimental and calculated adsorptions of CO<sub>2</sub>, CO, and N<sub>2</sub> at room temperature for DMOF-1.<sup>60</sup> They described the framework without charges and used Lennard-Jones parameters from the DREIDING force field. Within these assumptions, the simulated CO<sub>2</sub> isotherm of adsorption matches the experimental data. The chargeless framework better matches the low pressure experimental data from 1 to 15 bar than the isotherms calculated by Jiang et al. at the same conditions with a charged framework, which significantly

overestimate the low pressure adsorption.<sup>61</sup> Calculated isotherms from both Walton and Jiang converged to the same values at high pressures, where volume effects dominate the GCMC acceptance step.

### 2.2.1 Post-Synthetic Modification

Cohen and Wang found that post-synthetic modification of the BDC ligands within the DMOF-1 framework affects the pore size and breathing behavior. They showed that aminating the BDC ligands, forming DMOF-1-NH<sub>2</sub>, can lead to further modification at the free amino groups using anhydrides and isocyanates to form DMOF-1 with amide-linked alkyl chains.<sup>40</sup> These amide modifications of the DMOF-1 are called DMOF-1-AM<sub>n</sub>, where *n* corresponds to the number of carbons in the alkyl chain.

Figure 2.4 illustrates the AM1 to AM3 chains.

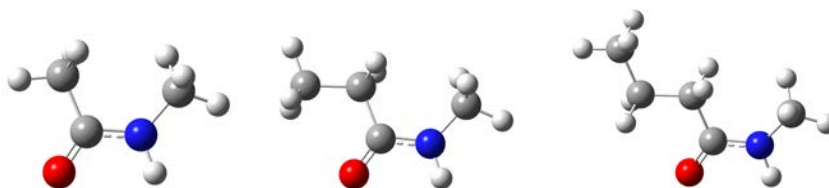


*Figure 2.4.* AM1 (*left*), AM2 (*middle*), and AM3 (*right*). Note that the methyl group capping the nitrogen is for illustration purposes only, and in reality it is connected to the DMOF-1 framework.

The alkyl chain length affects the DMOF-1-AM<sub>n</sub> pore size. The DMOF-1-AM<sub>n</sub> pore size can be inferred to be LP or NP from the amount of adsorbate uptake in the isotherms of adsorption. Cohen and Wang found that DMOF-1-AM1 through DMOF-1-AM3 at 196 K and low pressures correspond to NP structures.<sup>40</sup> Additionally,

DMOF-1-AM3 shows breathing behavior upon CO<sub>2</sub> adsorption. Amine chains longer than AM3 cause DMOF-1-AM $n$  to be always in the LP structure and consequently have more volume for additional CO<sub>2</sub> uptake.

# CHAPTER 3

## Methods

### 3.0 Introduction

The parameterization of a force field suitable for modeling the properties of DMOF-1 requires three steps: acquisition of atomic partial charges necessary to describe the electrostatic interactions, choice of a starting set of parameters for the bonded and non-bonded interactions, and tuning of the parameters to reproduce experimental data. This chapter introduces the ab initio methods used to calculate the partial atomic charges, as well as the molecular dynamics (MD) methods and force field parameters used in the simulations.

Ab initio calculations use different theoretical approaches to the electronic Schrödinger equation for a given molecular system. These theories use different approximations to represent the true Hamiltonian operator,  $H$ , which yields the total energy,  $E$ , when applied to a wave function,  $\psi$ , as shown in equation 1.

$$H|\psi\rangle = E|\psi\rangle \quad (1)$$

In this study, the levels of theory used are DFT and Møller-Plesset perturbation theory, which are discussed in sections 3.1 and 3.2, respectively.



MD is a method to calculate the mean energy value of a statistical ensemble by time averaging. In Section 3.6, each force field used to describe DMOF-1 and its adsorbents will be listed and the most important parameters will be discussed.

### 3.1 Density Functional Theory<sup>62</sup>

Within the Born-Oppenheimer approximation, the electronic Hamiltonian of molecular systems depends on the positions and charges of the nuclei as well as the number of electrons. This suggests that a useful physical observable for describing the electronic Hamiltonian is the density of electrons,  $\rho$ , which yields the total number of electrons on integration over all space and whose shape provides information about the charge of the nuclei. This idea was pursued by Hohenberg and Kohn, who first demonstrated that the electron density determines the ground state properties of a many-electron system. In a second theorem, Hohenberg and Kohn demonstrated that the variational principle also applies to the electronic energy expressed as a functional of the density according to

$$E[\rho] = E_0 \quad (2)$$

In equation 2,  $\psi_a$  is the wave function used and  $H_a$  is the Hamiltonian determined by the electron density being tested,  $E_a$  is the ground state energy determined by the tested Hamiltonian, and  $E_0$  is the true ground state energy.

The total energy derived from the electron density can be divided into different contributions shown in equation 3 where  $T$  is the total kinetic energy,  $V_{ee}$  is the electron-electron interaction,  $V_{nc}$  is the nucleus-electron interaction, and  $E_{xc}$  is the exchange-correlation energy.

$$E[\rho] = T[\rho] + V_{ee}[\rho] + V_{nc}[\rho] + E_{xc}[\rho] \quad (3)$$

As a first approximation, the exchange-correlation energy can be accounted for by the local density approximation (LDA), which assumes that  $E_{xc}[\rho]$  is a function of only the electronic density,  $\rho(r)$

A more accurate description of the exchange-correlation energy is obtained with hybrid DFT functionals that use a linear combination of exchange energy from LDA and Hartree-Fock (HF) theory. Among the different hybrid functionals the most popular functional being the B3LYP functional.<sup>62,63</sup> Since formally DFT scales as  $N^3$  while HF theory scales as  $N^4$ , where  $N$  is the number of basis set functions, discussed in Section 3.3. DFT is currently the only method capable of handling large numbers of electrons and, consequently, large numbers of atoms.

DFT has proven to be very useful for geometric optimization and calculations of ground state energy but is insufficient to determine excited state properties. DFT also does not account for weak interactions such as dispersion forces, and as such is unsuitable for accurately calculating adsorption energies, particularly when physisorption.

### 3.2 Møller-Plesset Perturbation Theory<sup>62</sup>

Møller-Plesset perturbation theory (MP $n$ ), where  $n$  indicates the level of perturbation, represents an effective methodology to add correlation effects to the HF solution of the electronic Schrödinger equation. This is accomplished through the use of the Rayleigh-Schrödinger perturbation theory.<sup>62</sup> Eiyhin MP $n$ , the electronic Hamiltonian,  $H$ , is separated into two contributions  $H^{(0)}$  and  $V$  according to

$$H = H^{(0)} + \lambda V \quad (2)$$

Where  $\lambda$  is a dimensionless parameter that is eventually set equal to 1. In equation 3,  $H^{(0)}$ , is the non-interacting Hamiltonian defined as the sum of the one-electron Fock operators,  $f_i$ , shown in equation 4.

$$H^{(0)} = \sum_{i=1}^n f_i \quad (4)$$

For each electron  $i$ , the Fock operator, defined in the Hartree-Fock theory, describes the electron kinetic energy as well as the electrostatic interactions between the electron  $i$  and all the nuclei, and between the electron  $i$  and the remaining  $N-1$  electrons ( $V_i^{\text{HF}}(j)$ ). This is shown in equation 5, where  $\Delta$  is the Laplace operator,  $Z_k$  is the nuclear charge, and  $r_{ik}$  is the nucleus–electron distance.

$$f_i = -\frac{1}{2}\Delta_i^2 - \sum_k^{\text{nuclei}} \frac{Z_k}{r_{ik}} + V_i^{\text{HF}}(j) \quad (5)$$

In equation 3,  $V$  corrects the non-interacting Hamiltonian to the true Hamiltonian using the difference between the correct instantaneous electron-electron energy,  $g(i,j)$ , and the mean-field value,  $V^{\text{HF}}$ , obtained in the Hartree-Fock theory.

$$V = \sum_{i<j}^N g(i,j) - \sum_{j=1}^N V^{\text{HF}}(j) \quad (6)$$

Due to the nature of the electron-electron interactions, which depends only on the coordinates of two electrons, MP2 is the minimum useful level of perturbation required to improve on the Hartree-Fock solution and recover part of the correlation energy.

In general, MP perturbation theory overestimates dispersion interactions and should be used with some caution in calculation of binding energies. MP theory in general provides a more accurate description of the electronic properties of a molecular system than DFT, but is also more computationally expensive, scaling as  $N^5$ , which limits its use in relatively large systems. Furthermore, contrary to DFT, MP theory is not variational, which implies that the  $MPn$  energies can be both larger and smaller than the correct energy.

### 3.3 Basis Sets<sup>62</sup>

A basis set is a set of functions that represent atomic orbitals, and are used to describe the wavefunction in the Schrödinger equation. In principle, a complete basis set consists of an infinite number of functions, which is computationally impossible. As a finite basis set approaches the accuracy of an infinite basis set, it is said to approach the basis set limit. The computing time scales with the number of basis set functions. As mentioned above, DFT scales as  $N^3$  and HF as  $N^4$ . It is thus desirable to have as small of a basis set as possible without jeopardizing the accuracy of the final result. A minimum basis set is the smallest basis set required to contain all of the electrons in the system, e.g. first row elements require a single s-function and second row elements require an additional set of 2s and p functions.

Several types of equations can represent atomic orbitals. Slater Type Orbitals (STOs), shown in equation 7, exactly mirror the exponential decay of the electron density from the nucleus as well as the shape of the density close to the nucleus. However, they suffer from a fairly significant limitation, since there is no analytical solution available for the Coulomb and exchange integrals when the basis functions are STOs.

$$\chi_{\zeta,n,l,m}(r,\Theta,\varphi) = NY_{l,m}(\Theta,\varphi)r^{n-l}e^{-\zeta r} \quad (7)$$

In equation 7,  $N$  is a normalization constant and  $Y_{l,m}$  is the appropriate spherical for the quantum numbers  $l$  and  $m$ . In practical calculations, it is generally preferable to use

Gaussian Type Orbitals (GTOs) because they facilitate the integration of the Coulomb and exchange integrals that appear in the solution of the Schrödinger equation of an  $n$ -electron system. GTOs are expressed as

$$\chi_{\zeta,n,l,m}(r,\Theta,\varphi) = NY_{l,m}(\Theta,\varphi)r^{2n-2-l}e^{-\zeta r^2} \quad (8)$$

However, GTOs also suffer from some limitations. In particular, the  $r^2$  term causes the GTO to decay too quickly, resulting in a too shallow electron density at longer radial distances. Also, at the nucleus the slope of the GTO is zero whereas the STO is correctly discontinuous. It has been shown that a linear combination of three GTO is able to reproduce the main features one STO. Additional functions can also be used to improve the accuracy of GTOs. For example, Double Zeta (DZ) type basis sets double the number of basis functions used, e.g. DZ hydrogen has two s-type functions to describe the actual 1s orbital. Following the same procedure, it is possible to construct larger basis sets by using 3(Triple Zeta), 4(Quadruple Zeta), etc. functions for each actual atomic orbital. Since in a molecular system the core electrons are mostly independent of the surrounding chemical environment, it has been shown that an accurate description of the electron density can be obtained by splitting the number of basis functions of only the valence electrons. This leads to the so-called split valence basis sets.

In order to better describe the shape of the electron density upon the formation of chemical bonds, the basis sets also include polarization functions, which are higher angular momentum functions that aid in correctly modeling chemical bonds. For example, a p-function on a hydrogen atom can help represent the electron distribution

along a H–C bond that is more localized in the direction of the bond than an isotropic orientation, which an s-function represents. Several polarization functions may be required to correctly represent correlation effects. Finally, diffuse functions can also be added to a basis set and are particularly important for describing loosely bound electrons, excited states, and anions. In general, diffuse functions have small exponential terms that do not decay rapidly with the distance from the nucleus and, therefore, better describe the electron density at large distances.

Due to the large number of electrons, metals and other heavy elements pose a challenge in that many basis functions are required to describe them. However, many of the additional core electrons can be described relatively simply. Hellmann proposed the idea to replace these electrons with analytic functions that effectively represent nuclear-electronic core interactions, referred to as effective core potentials (ECPs).<sup>62</sup> A popular set of pseudopotentials used to describe first row transition metals is the Los Alamos National Laboratory (LANL) ECPs.<sup>62</sup>

### 3.3.1 Basis Set Superposition Error<sup>64</sup>

In weakly bound molecular complexes, an unphysical lowering of energy often occurs due to the so-called “basis set superposition error.” This arises from an asymmetric use of basis sets between the bound and separated molecules. This is illustrated by considering the combination of two fragments, A and B, that form the complex A•B. The binding energy,  $\Delta E_{bind}$ , is the energy difference between the

complex and the fragments as illustrated in equation 9, where the superscripts indicate the basis set associated to each fragment (A and B) and the molecular complex (A•B).

$$\Delta E_{bind} = E^{AB}(A \bullet B) - (E^A(A) + E^B(B)) \quad (9)$$

The complex A•B has a basis set that is the sum of the fragment basis sets *A* and *B*. For example, if the basis sets of A and B are represented by 10 basis functions each, then the complex A•B is represented by 20 basis functions. The difference in the number of functions that are effectively used to describe the molecular complex and the two fragments gives rise of the basis set superposition error. The counterpoise correction technique is used to approximately compensate for this error.<sup>62</sup> In this procedure, the correction to the basis set superposition error associated to each fragment,  $E_{BSSE}$ , is defined as the difference of the energy calculated with the expanded basis set of the complex and that obtained with the fragment basis set.

$$E_{BSSE}(A) = \square^{AB}(A) - E^A(A) \quad (10)$$

$$E_{BSSE}(B) = E^{AB}(B) - E^A(B) \quad (11)$$

The energies  $E_{BSSE}(A)$  and  $E_{BSSE}(B)$  are then subtracted from equation 9 to correct for the basis set superposition error.



### 3.4 Partial Charge Determination

The concept of atomic partial charges is useful to describe the polarity within molecular systems. For purpose of simulating large systems, it is desirable to simplify the electron density into single, atom-centered, non-polarizable monopole charges. These are usually fitted to reproduce physically meaningful properties such as the dipole and quadrupole moments, and the electrostatic potential. Because the atomic partial charges are not quantum observable, a variety of methods exist for their determination.<sup>65-68</sup> In this study, only the methods that are relevant to model MOFs will be discussed. The electrostatic potential (ESP) is a molecular property that can be directly calculated using ab initio methods and can be expressed effectively in terms of a set of atom-centered monopoles.

#### 3.4.1 CHELP<sup>69</sup>/CHELPG<sup>70</sup>

CHarges from ELectrostatic Potentials (CHELP) is a method that determines a set of monopole charges by optimizing the least squares fit of the charges to the ESP. According to this, the electrostatic potential is calculated at numerous points around each atomic center, excluding all points within the van der Waals radii. An iterative procedure is then employed to obtain the best set of atomic partial charges that reproduce the electrostatic potential.

CHELP is known to have significant orientation-dependent charge fluctuations that occur as an artifact of the ESP point selection. CHarges from ELectrostatic

Potential with Grid (CHELPG) uses a grid-based method to more selectively and densely sample the space around each atomic center to yield more reliable charges. In principle, the accuracy of this method increases with higher levels of theory, larger basis sets, and denser sampling. CHELPG is one of the most popular partial charge methods and is used in this study.

Optimizing the least squares fit can have several issues that skew the charge accuracy. With large numbers of atoms, the charge distribution tends to “smear” and the differences between one set of charges and another becomes very small. However, as long as there are many more points than charges to be determined, it is assumed that sufficient data exists to successfully minimize the root mean square deviation of the monopole approximation. The accuracy of the monopole fitting relies on the independence of each ESP calculation. This assumption of independence is often incorrect, and there is a high degree of linear dependence in the least squares matrix rendering it highly rank deficient.<sup>71</sup> In general, the number of linearly independent rows or columns defines the rank of a matrix. In CHELP and CHELPG applications, the rank is determined as the number of independent points used for the ESP fitting. Denser point distribution is often thought to increase the rank but is not always so. Naturally, increasing the size of the basis set and level of theory makes the ESP calculation more accurate but does not increase the rank of the problem. These errors are inherent within the CHELP and CHELPG models and will not be addressed within this study.

### 3.5. Ab Initio Calculations

Gaussian 09 was used for all quantum chemistry calculations.<sup>42</sup> Unless otherwise specified, the CHELPG method with a cc-PVDZ<sup>72,73</sup> basis set was used to determine the atomic partial charges.

#### 3.5.1 1,4-Benzenedicarboxylate

The BDC ligand was investigated by first optimizing the structure then using it to obtain the corresponding set of atomic partial charges. The optimization was conducted using both an isolated BDC, and a BDC connected to two truncated Zn clusters, as shown in Figure 3.1. In general, truncated metal clusters capped with carboxylates have been shown to provide a reasonable representation of the metals.<sup>74</sup> For the isolated BDC, the levels of theory used in the optimizations were the B3LYP and M062X<sup>75</sup> DFT functionals, and MP2 perturbation theory. Since the BDC-cluster contains many more atoms, including metals, the optimizations were conducted using only the B3LYP and M062X DFT functionals, with and without the LAN2DZ ECP basis set on the Zn atoms. In general, optimizations of truncated clusters cannot be conducted via MP2 or higher levels of theory because of the large number of electrons and associated basis sets. The Zn–Zn distance, Zn–O distance, and Zn–O–C angle were compared for each optimization to determine which functional is best suited to reproduce the crystal structure of DMOF-1.

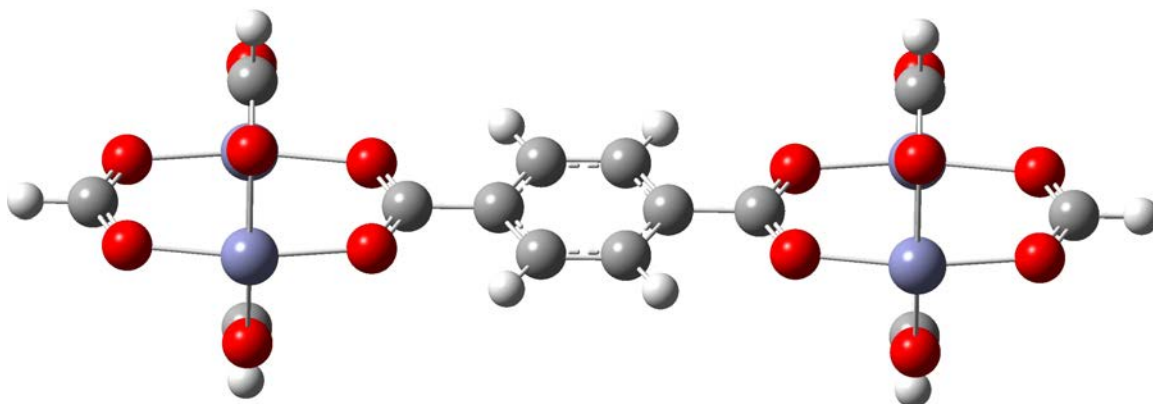


*Figure 3.1.* The BDC-cluster to be optimized. The truncated Zn-clusters were capped with  $\text{HCO}_2^-$  for charge neutrality. O = red, Zn = purple, C = grey, H = white.

The charge distribution was investigated by conducting single point energy calculations on the M062X optimized structure with the B3LYP and M062X DFT functionals, and MP2 perturbation theory. It is a common practice to first optimize large structures with a lower level of theory and then calculate partial charges with a single point energy calculation using a higher level of theory.<sup>74</sup> The partial charges between the isolated BDC and the BDC-cluster were compared to determine the impact of the metal clusters on the BDC ligand and find the charge transfer between the two. The differences between the DFT functionals and MP2 perturbation theory were compared to determine the necessity of using higher levels of ab initio theory for partial charge determination. For the truncated cluster, the charges were calculated using a Zn

van der Waals radius cutoff of 1.00 Å. Commonly used Zn radii vary between 1.00 and 2.00 Å.<sup>74</sup>

After the BDC partial charges were determined, the Zn–O bond force constant was required to be calculated prior to simulation. An energy scan of the Zn–O bond was conducted by varying the Zn–O bond connections between the BDC and the Zn–cluster equally. At 0.1 Å intervals from 1.5 to 4.8 Å, the scan was investigated at the MP2 level of theory using the counterpoise correction.<sup>30,62</sup> In order to determine the force constant, resulting potential energy curve was appropriately divided by two to remove double counting of the interactions and fit to a harmonic potential.

### 3.5.2 Post-Synthetically Modified BDC

Post-synthetically modified BDC ligands with amide chains were studied with and without truncated metal clusters similarly to the unmodified BDC ligand. The amine modified BDCs will be referred to as “BDC-AM $n$ ” where  $n$  is the length of the alkyl chain. Isolated ligand optimizations were conducted for BDC-AM1 to BDC-AM6 with the B3LYP and M062X DFT functionals and MP2 perturbation theory.

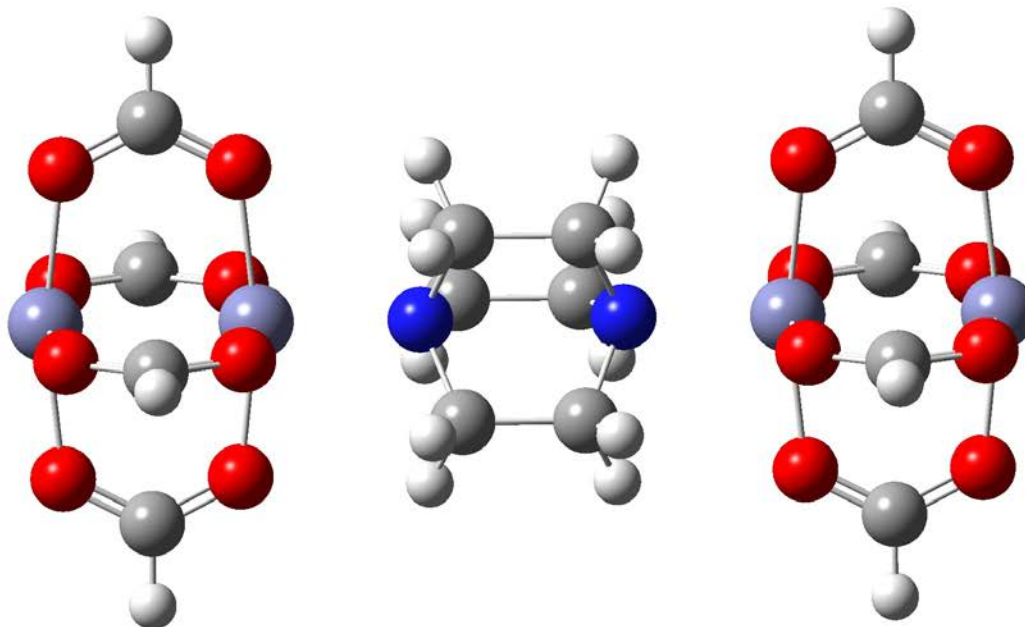
Partial optimizations, which keep all atoms fixed except those of the amide, were performed on BDC-AM1 to BDC-AM6 with the truncated Zn–clusters using the B3LYP functional. The BDC and Zn clusters were frozen in the M062X optimized positions previously calculated for the BDC–cluster. The partial charges were investigated using the MP2 level of theory with the LAN2DZ ECP basis set on the Zn atoms. Partial charges of the individual amide chains capped with a methyl group as in

Figure 2.4 were also calculated at the MP2 level of theory. The partial charges for the isolated chains were used later in this study to represent chains longer than AM1.

### 3.5.3. DABCO

The DABCO ligand was investigated analogously to the BDC ligand by first optimizing the structure and using it to determine the corresponding set of atomic partial charges. The single ligand optimizations were conducted using the B3LYP and M062X DFT functionals, and MP2 perturbation theory. A truncated cluster, as was previously seen, was optimized using the “int=ultrafine” keyword in Gaussian 09 to assist with energy convergence.

In order to simulate the Zn–N bond, the bond constant was determined by fitting the corresponding bond potential. An energy scan of the Zn–N bond was conducted by varying the Zn–N length of one Zn cluster between 1.5 to 5 Å with 0.1 Å intervals. Figure 3.2 shows the DABCO–cluster. In these calculations, the DABCO was kept fixed at its optimal geometry obtained at the MP2 level of theory. The energy scan was calculated with the counterpoise correction at the MP2 level of theory, as well as with the M062X functional. At each step, the atomic partial charges were obtained with a Zn van der Waals radius cutoff of 1.00 Å. In order to determine the force constant, the well minimum was fit to a harmonic potential.



*Figure 3.2.* An illustration of the DABCO–cluster where the DABCO is bound to two Zn clusters.

### 3.6 Molecular Dynamics

MD moves all simulated atoms according to Newton’s laws of motion, which are often propagated in time using a velocity Verlet algorithm with a time step,  $\Delta t$ .<sup>30</sup> Predetermined force fields completely describe the nature of the interaction of each atom with every other atom. The energy associated with the bonds is represented by two-body potentials often described via a harmonic potential shown in equation 12, where  $r_0$  is the equilibrium bond distance in Å.

$$E_{bonds} = \frac{K}{2}(x - r_0)^2 \quad (12)$$

Possible improvements on the description of the bonds include the use of anharmonic potentials, Morse potential, and/or cross terms that depend on the values of the angles that are associated with the specific bond.

The energy associated with the angles is represented by three-body potentials that, like the bonds, are often described with harmonic potentials. As with the bonds, the description of the angle can be improved using anharmonic potentials and/or cross terms.

The energy associated with the dihedral angles is represented by four-body potentials between atoms ABCD. Using this notation, the dihedral angle is the angle between the bonds AB and CD when they are projected onto the plane bisecting the BC bond.<sup>62</sup> The angle is defined to be positive if the bond in front of the bisecting plane must be rotated clockwise to eclipse the bond behind the bisecting plane. Dihedral potentials can also be described using harmonic potentials. However, this representation does not satisfy the natural periodicity. Therefore, the dihedral angles are usually modeled via periodic functions such as that shown in equation 13, where A is a parameter proportional to the strength of the potential, m is the periodicity,  $\theta$  is the angle, and  $\delta$  is the equilibrium angle.

$$E_{\text{Dihedral}} = A[1 + \cos(m\theta - \delta)] \quad (13)$$

The van der Waals interactions are usually described by Lennard-Jones potentials,  $E_{\text{LJ}}$



$$E_{LJ} = 4\varepsilon\left[\left(\frac{\sigma}{r}\right)^{12} - \left(\frac{\sigma}{r}\right)^6\right] \quad (14)$$

where  $\varepsilon$  is the potential well depth and  $\sigma$  is the distance of which  $E_{LJ}=0$ . The Morse and Hill potentials are other common functions used to describe the van der Waals interactions.<sup>62</sup>

Molecular dynamics is an effective methodology for sampling the phase space of a molecular system using a particular statistical ensemble.<sup>30</sup> The phase space is position-momentum space that is  $6N$  dimensional, where  $N$  is the number of particles. The ergodic hypothesis<sup>30,62</sup> indicates that for a sufficiently long phase space trajectory at constant energy, each region of the phase space will be sampled equally often. As a result of equal sampling over time, the time average converges to the true average. This is a reasonable assumption for systems that do not have free energy barriers much larger than  $kT$ , which is the case in the current study. If free energy barriers greater than  $kT$  exist, it is possible that the simulation is only sampling energies at a local energy minima, while the global energy minimum will never be sampled within the constraints of the simulation time.

In a constant volume ensemble (NVT) the number of atoms, volume, and temperature are held constant. The constant volume fixes the unit cell vectors such that they do not change over the course of the simulation. Likewise, in a constant pressure ensemble (NPT) the number of atoms, pressure, and temperature are held constant while the unit cell vectors are allowed to change. The change in the unit cell vectors are defined by the pressure tensor that is derived from the intermolecular and

intramolecular forces of the system. The NPT ensemble is therefore suitable for flexible systems such as MOFs and will allow the breathing motion to be observed during the simulation.

### 3.6.1 Non-Bonded Type Force Fields

Non-bonded and restrained force fields, described below, were created and used to model DMOF-1 using the AMBER 11 MD package. The force field parameters listed in Tables 3.1A to 3.1D were used. The simulations were run at 223 K and 1 bar outputting statistics every 500 steps unless otherwise specified. In the AMBER simulations the diagonal elements of the pressure tensor are used to determine the pressure. As a consequence, the simulation box can only contract or expand but cannot change its shape.

The temperature and pressure controls in the simulations of DMOF-1 and DMOF-1+2BEN were attained using a thermostat and a barostat with relaxation times of 20 ps and 0.1 ps, respectively. However, it was found that these the choice of relaxation times did not affect the results noticeably. The benzene force field parameters and charges were taken from the GAFF and All atom databases. Figure 3.3 shows the atom labels for the DMOF-1 framework using GAFF database labeling scheme.

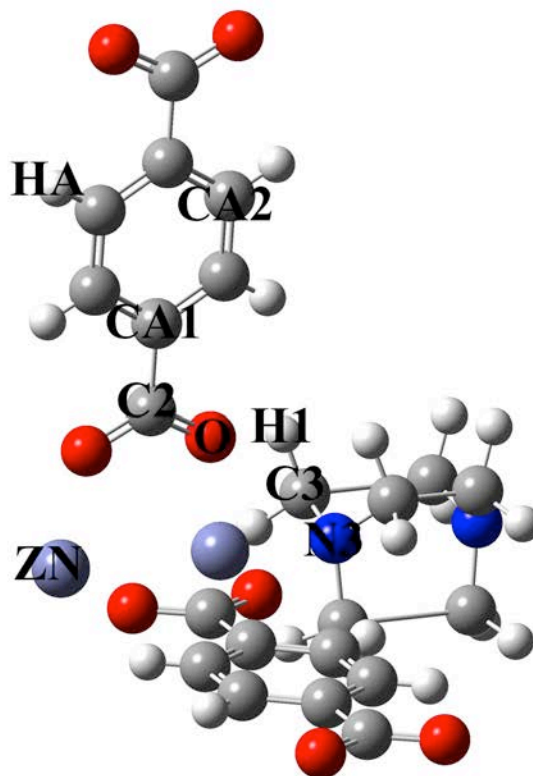


Figure 3.3. A unit cell of DMOF-1 showing the atomic labels.

Table 3.1A. Bonds used within the non-bonded type force fields for the DMOF-1 framework.

Bonds (ligand)	Force Const. (kcal mol <sup>-1</sup> Å <sup>-2</sup> )	Position (Å)
O-C2 (BDC)	1092.4	1.26
C2-CA (BDC)	714.4	1.48
CA-CA (BDC)	956.8	1.39
CA-HA (BDC)	688.6	1.09
N3-C3 (DABCO)	641.2	1.47
C3-H1 (DABCO)	671.8	1.09
C3-C3 (DABCO/PSM)	606.2	1.53
HN-N (PSM)	820.4	1.01
N-C2 (PSM)	781.0	1.41
N-CA (PSM)	744.6	1.42
C2-C3 (PSM)	656.6	1.51
C3-HC (PSM)	674.6	1.09
C2-HC (PSM)	686.6	1.09

Table 3.1B. Angles used within the non-bonded type force fields for the DMOF-1 framework.

Angles (ligand)	Force Const. (kcal mol <sup>-1</sup> rad <sup>-2</sup> )	Position (°)
O-C2- O (BDC)	155.8	121.69
O-C2-CA (BDC)	138.4	119.78
C2-CA-CA (BDC)	129.4	120.60
CA-CA-HA (BDC)	97.0	120.01
CA-CA-CA (BDC)	134.4	119.97
C3-C3-N3 (DABCO)	132.4	110.38
C3-N3-C3 (DABCO)	128.0	110.90
H1-C3-H1 (DABCO)	78.4	109.55
H1-C3-N3 (DABCO)	98.8	109.92
C3-C3-H1 (DABCO/PSM)	92.7	110.07
HC-C3-HC PSM)	78.8	108.35
C3-C2-O (PSM)	138.2	116.88
C2-C3-HC (PSM)	94.0	110.49
C2-N-HN (PSM)	94.9	117.86
C3-C2- N (PSM)	133.5	113.88
N-C2-O (PSM)	148.2	117.46
CA-N-HN (PSM)	95.2	117.46
C2-N-CA (PSM)	129.8	116.54
CA-CA-N (PSM)	136	119.89
C3-C3-HC (PSM)	92.8	110.05
C3-C3-C3 (PSM)	126.4	110.63
C2-C3-C3 (PSM)	127.4	110.96

Table 3.1C. Dihedrals used within the non-bonded type force fields for the DMOF-1 framework.

Dihedrals (ligand)	Force Const. (kcal mol <sup>-1</sup> )	Position (°)	Periodicity
C3-C2-N-HN (BDC)	0.650	180	2
HA-CA-CA-N (PSM)	3.625	180	2
H1-C3-C3-H1 (DABCO/PSM)	0.156	0	3
C3-N3-C3_H1 (DABCO)	0.156	0	3
C3-C3-N3-C3 (DABCO)	0.480	180	2
CA-CA-N-HN (PSM)	0.450	180	2
CA-CA-C2-O (BDC)	2.550	180	2
C2-CA-N-HN (PSM)	1.100	180	2
HC-C3-C3-O (BDC)	0.000	180	2
CA-O-C2-O (BDC)	1.100	180	2
CA-CA-CA-HA (BDC)	3.625	180	2
CA-CA-CA-N (PSM)	3.625	180	2
C3-N-C2-O (PSM)	1.100	180	2
HA-CA-CA-HA (BDC)	3.625	180	2
CA-CA-CA-CA (BDC)	3.625	180	2
HA-CA-CA-C2 (BDC)	3.625	180	2
N-CA-CA-C2 (PSM)	3.625	180	2
HC-C3-C3-HC (PSM)	0.250	0	3
C3-C3-C3-HC (PSM)	0.160	0	3
C3-C3-C3-C3 (PSM)	0.200	180	1
C3-C3-C3-C3 (PSM)	0.250	180	2
C3-C3-C3-C3 (PSM)	0.180	0	3

Table 3.1D. Lennard-Jones parameters for the GAFF database atom types.

Atom Type	Epsilon (kcal mol <sup>-1</sup> )	Sigma (Å)
ZN	0.0125	1.2472
O	0.2100	1.4800
C2	0.0860	1.6998
CA	0.0860	1.6998
HA	0.0150	1.2998
N3	0.1700	1.6250
H1	0.0157	1.2357
HC	0.0157	1.3248
C3	0.1094	1.6998
N	0.1700	1.6250
HN	0.0150	0.5345

### 3.6.1.1 Fully Non-Bonded Force Field

DMOF-1 was first investigated by using a non-bonded force field that describes the Zn–O and Zn–N bonds only in terms of electrostatic interactions. This is the most basic type of force field used in this study. Although the bond potential is not correctly represented, a non-bonded force field has the distinct advantage of breakable Zn–ligand bonds that are otherwise impossible with a fully-bonded force field. The effects of different charges listed in Table 3.2 were first investigated using the evacuated framework then tuning the Zn van der Waals radius ( $R_0 = \sqrt[6]{2}\sigma$ ) to fit the Zn–O bond length. The M062X derived charges using the isolated BDC and DABCO ligands were first simulated with a Zn radius of 1.1 Å for 500 ps using 27 unit cells with a cutoff of 12 Å for the non-bonded interactions. Charges derived using isolated ligands were the least accurate, so the charges derived using the BDC-cluster at the MP2 level of theory with the LAN2DZ ECP basis set was used with a Zn radius of 1.1 Å. The model with

MP2-derived charges was simulated using 16 unit cells with a 9 Å cutoff for 2 ns. Both simulations were rerun using an increased Zn radius of 1.4 Å to better reproduce the Zn–O bond length.

DMOF-1+2BEN was simulated with periodically distributed benzene molecules into 16 unit cells using a 9 Å cutoff. The framework partial charges were derived with the BDC-cluster model at the MP2 level of theory with the LAN2DZ ECP basis set. The charges used on the benzene CA and HA atoms are +0.15 and -0.15. The benzene force field parameters are listed in Tables 3.3A to 3.3C.

Table 3.2. Two sets of partial charges used with DMOF-1

Charges (ligand)	(M062X) 2+ formal	(MP2) bdc-cluster
ZN	2.000000	1.475000
O (BDC)	-0.708664	-0.713315
C2 (BDC)	0.586963	0.646910
CA (BDC)	-0.051466	0.073876
CA2 (BDC)	-0.138162	-0.129946
HA (BDC)	0.079078	0.114118
H1 (DABCO)	0.075543	0.003494
N3 (DABCO)	-0.421501	-0.515610
C3 (DABCO)	-0.010586	0.163882

Table 3.3A. Bonds used in the benzene force field.

Bonds	Force Const. (kcal mol <sup>-1</sup> Å <sup>-2</sup> )	Position (Å)
CA-CA	956.8	1.39
CA-HA	688.6	1.09

Table 3.3B. Angles used in the benzene force field.

Angles	Force Const. (kcal mol <sup>-1</sup> rad <sup>-2</sup> )	Position (°)
CA-CA-HA	97	120.01
CA-CA-CA	134.4	119.97

Table 3.3C. Dihedrals used in the benzene force field.

Dihedrals	Force Const. (kcal mol <sup>-1</sup> )	Position (°)	Periodicity
HA-CA-CA-HA	3.625	180	2
CA-CA-CA-CA	3.625	180	2
CA-CA-CA-HA	3.625	180	2

DMOF-1-AM1 to DMOF-1-AM4 were studied with the same parameters as DMOF-1 at 196 K, which corresponds to the temperature of the experiments of Cohen and Wang.<sup>40</sup> The chains were randomly distributed on the framework with one chain per BDC to reproduce the experimental conditions. The charges used with BDC-AM1 were derived using the BDC-AM1–cluster model at the MP2 level of theory with LAN2DZ basis set. Figure 3.4 shows the labeling scheme for the AM1 atoms and Table 3.4 lists the corresponding partial charges. The simulation was run for 2 ns using 16 unit cells and a 9 Å cutoff. The charges used with the AM2 to AM4 alkyl chains were derived from MP2-level calculations on the individual amine chains using the BDC-AM1–cluster charges for the rest of the framework. Figure 3.5 shows the labeling scheme for AM2 to AM4 while Table 3.5 lists the corresponding charges.



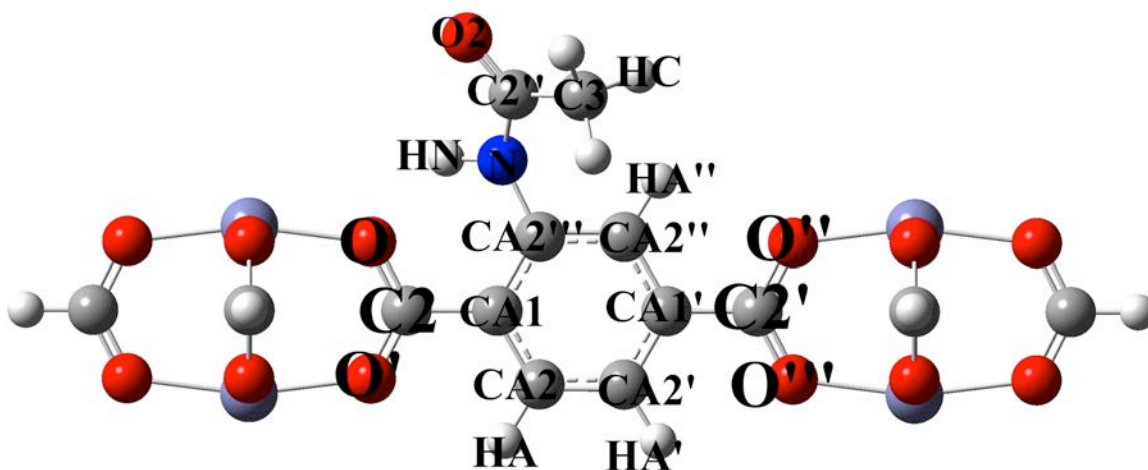


Figure 3.4 BDC-AM1-cluster labels.

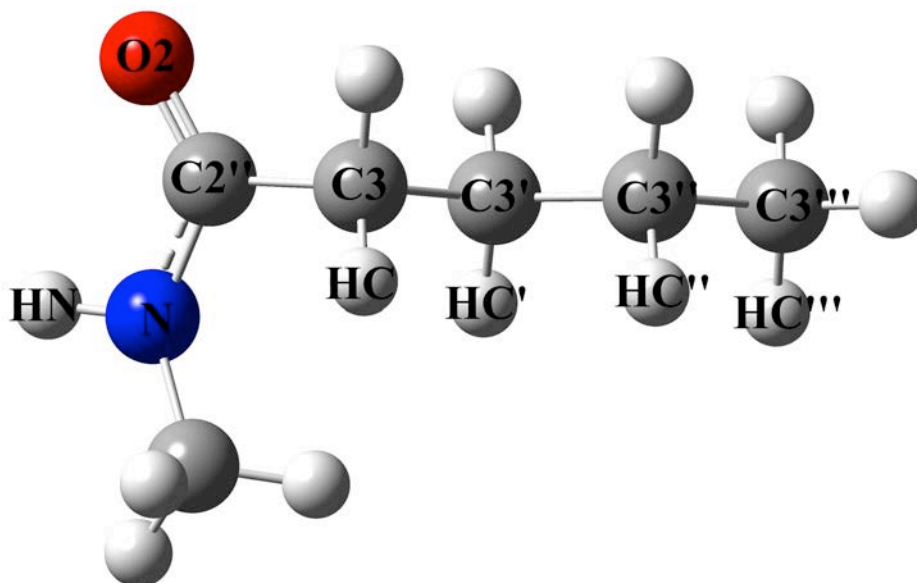


Figure 3.5. Isolated AM4 illustrating the labeling scheme. Atoms of the same type are distinguished with different numbers of apostrophes.

Table 3.4. Partial charges on atoms of BDC-AM1-cluster

Atom	Charges
O1	-0.7102
O2	-0.7200
O3	-0.7268
O4	-0.7256
C2	0.7023
C2'	0.6765
CA1	-0.0823
CA1'	0.1028
CA2	-0.1114
CA2''	-0.7727
CA2'''	-0.2846
CA2''''	0.3364
HA	0.1287
HA'	0.1285
HA''	0.1686
N	-0.6767
HN	0.3602
C2''	0.7175
O5	-0.5461
C3	-0.2175
HC	0.0606
ZN	1.2090

Table 3.5. Atomic charges of the AM2 to AM4 alkyl chains. Charges on atoms not present in an amine group are labeled with n/a.

Atom	AM2	AM3	AM4
C3	0.1105	-0.0397	-0.1068
HC	-0.0372	-0.0024	0.0166
C3'	-0.0936	0.1997	0.0654
HC'	0.0073	-0.0463	-0.0155
C3''	n/a	-0.1648	0.1878
HC''	n/a	0.0222	-0.0460
C3'''	n/a	n/a	-0.1956
HC'''	n/a	n/a	0.0344

### 3.6.1.2 Restrained Force Field

Since the non-bonded force field proved to be too flexible, so harmonic potentials were used to restrain the flexibility around the Zn clusters. This model is called the “restrained force field”. The Zn–O–C angles were restrained at  $111.12^\circ$  with  $31.664 \text{ kcal mol}^{-1} \text{ rad}^{-2}$  force constants. The Zn–O–C–C dihedrals were restrained at  $180^\circ$  with  $3.37 \text{ kcal mol}^{-1}$  force constants. DMOF-1+2BEN was simulated at 223K for 4 ns with a 1 fs time step and statistics outputted every 500 steps. A 9 Å cutoff was used and the system consisted of 16 unit cells. DMOF-1-AM1 to DMOF-1-AM4 were studied at the experimental temperature of 196 K. The chains were randomly distributed on the framework with one chain per BDC as in the non-bonded force field.

### 3.6.2 Fully-Bonded Force Field

Although AMBER is a highly efficient MD package, it has two primary issues with creating a fully-bonded force field: the creation of bonds that go through periodic boundary conditions, and the impossibility of modifying the shape of the simulation box in NPT simulations. The DL\_POLY\_4 MD package solves all of these issues. Additionally, DL\_POLY\_4 has more types of potentials that can represent bonds, angles, and dihedrals.

The fully-bonded force field parameters used in the present study are listed in Tables 3.6A–D. The Lennard-Jones parameters used are the same as in Table 3.2.

Table 3.6A. Bond parameters for the fully-bonded force field.

Bonds (ligand)	Force Const. (kcal mol <sup>-1</sup> Å <sup>-2</sup> )	Position (Å)
ZN-O	280.4	2.03
ZN-N3	140.8	2.07
ZN-ZN	36.0	2.50
O-C2 (BDC)	1092.4	1.26
C2-CA (BDC)	714.4	1.48
CA-CA (BDC)	956.8	1.39
CA-HA (BDC)	688.6	1.09
N3-C3 (DABCO)	641.2	1.47
C3-H1 (DABCO)	671.8	1.09
C3-C3 (DABCO/PSM)	606.2	1.53
HN-N (PSM)	820.4	1.01
N-C2 (PSM)	781.0	1.41
N-CA (PSM)	744.6	1.42
C2-C3 (PSM)	656.6	1.51
C3-HC (PSM)	674.6	1.09
C2-HC (PSM)	686.6	1.09

Table 3.6B. Angle parameters for the fully-bonded force field.

Angles (ligand)	Force Const. (kcal mol <sup>-1</sup> rad <sup>-2</sup> )	Position (°)
ZN- O-C2 (BDC)	5.00	125.54
O-ZN- O (BDC)	30.76	99.45
O-ZN- O (BDC)	30.76	88.45/ 161.10
O-C2- O (BDC)	155.80	121.69
O-C2-CA (BDC)	138.44	119.785
C2-CA-CA (BDC)	129.4	120.60
CA-CA-HA (BDC)	97.00	120.01
CA-CA-CA (BDC)	134.40	119.97
C3-C3-N3 (DABCO)	132.36	110.38
C3-N3-C3 (DABCO)	128.02	110.9
H1-C3-H1 (DABCO)	78.36	109.55
H1-C3-N3 (DABCO)	98.78	109.92
C3-C3-H1 (DABCO/PSM)	92.72	110.07
HC-C3-HC PSM)	78.80	108.35
C3-C2-O (PSM)	138.20	116.88
C2-C3-HC (PSM)	94.00	110.49
C2-N-HN (PSM)	94.90	117.86
C3-C2- N (PSM)	133.54	113.875
N-C2-O (PSM)	148.15	117.46
CA-N-HN (PSM)	95.20	117.46
C2-N-CA (PSM)	129.80	116.54
CA-CA-N (PSM)	136.00	119.89
C3-C3-HC (PSM)	92.80	110.05
C3-C3-C3 (PSM)	126.40	110.63
C2-C3-C3 (PSM)	127.40	110.96

Table 3.6C. Dihedral parameters for the fully-bonded force field.

Dihedrals (ligand)	Force Const. (kcal mol <sup>-1</sup> )	Position (°)	Periodicity
ZN-O-C2-CA (BDC)	1.640	180	2
ZN-O-C2-O (BDC)	1.640	180	2
O-ZN-CA-CA (BDC)	0.000	180	2
C3-C2-N-HN (BDC)	0.650	180	2
HA-CA-CA-N (PSM)	3.625	180	2
H1-C3-C3-H1 (DABCO/PSM)	0.156	0	3
C3-N3-C3_H1 (DABCO)	0.156	0	3
C3-C3-N3-C3 (DABCO)	0.480	180	2
CA-CA-N-HN (PSM)	0.450	180	2
CA-CA-C2-O (BDC)	2.550	180	2
C2-CA-N-HN (PSM)	1.100	180	2
HC-C3-C3-O (BDC)	0.000	180	2
CA-O-C2-O (BDC)	1.100	180	2
CA-CA-CA-HA (BDC)	3.625	180	2
CA-CA-CA-N (PSM)	3.625	180	2
C3-N-C2-O (PSM)	1.100	180	2
HA-CA-CA-HA (BDC)	3.625	180	2
CA-CA-CA-CA (BDC)	3.625	180	2
HA-CA-CA-C2 (BDC)	3.625	180	2
N-CA-CA-C2 (PSM)	3.625	180	2
HC-C3-C3-HC (PSM)	0.250	0	3
C3-C3-C3-HC (PSM)	0.160	0	3
C3-C3-C3-C3 (PSM)	0.200	180	1
C3-C3-C3-C3 (PSM)	0.250	180	2
C3-C3-C3-C3 (PSM)	0.180	0	3

DMOF-1 was simulated at 223 K and 1 bar for 2 ns using a thermostat and a barostat with relaxation times of 5 and 1 ps, respectively. A 9 Å cutoff was used and the system consisted of 16 unit cells. These values correspond to the thermostat and barostat relaxation times that Ferey et al. used to simulate the breathing of MIL-53 in DL\_POLY.<sup>37</sup> The charges used for the framework were derived from the BDC-cluster

and DABCO-cluster models calculated at the MP2 level of theory and the LAN2DZ basis set. A 1 fs timestep was used with statistics outputted every 200 steps. DMOF-1+2BEN was simulated for 7.5 ns under the same conditions as DMOF-1. The benzene force field was the same as in the AMBER simulations. The amount of benzene per unit cell was varied from 1 to 2 at 0.25 increments and simulated for 1 ns each. Using the same protocol, one to four isopropyl alcohol molecules (IPA) per unit cell were also simulated at the experimental temperature of 308 K.<sup>51</sup> The IPA force field parameters are listed in Tables 3.7A to 3.7D. The benzene and IPA simulations were equilibrated for 100 ps in the NVT ensemble prior to performing the production runs in the NPT ensemble. DMOF-1-AM1 to DMOF-1-AM4 were simulated using the same protocol at the experimental temperature of 196 K for 4 ns.<sup>40</sup> In this case, 32 unit cells and a 12 Å cutoff were used and the alkyl chains were randomly distributed within the framework.

*Table 3.7A.* Bonds for the IPA force field.

Bonds	Force Const. (kcal mol <sup>-1</sup> Å <sup>-2</sup> )	Position (Å)
C3-OH	628.2	1.426
OH-HO	739.2	0.974
C3-HC	674.6	1.092
C3-H1	671.8	1.09

Table 3.7B. Angles for the IPA force field.

Angles	Force Const. (kcal mol <sup>-1</sup> rad <sup>-2</sup> )	Position (°)
C3-C3-OH	135.44	109.43
H1-C3-OH	101.94	109.88
C3-OH-HO	94.18	108.16
HC-C3-HC	78.8	108.35
C3-C3-HC	92.8	110.05
C3-C3-C3	126.4	110.63
C3-C3-H1	92.72	110.07

Table 3.7C. Dihedrals for the IPA force field.

Dihedrals	Force Const. (kcal mol <sup>-1</sup> )	Position (°)	Periodicity
C3-C3-OH-HO	0.25	0	1
C3-C3-OH-HO	0.16	0	3
HC-C3-C3-OH	0	0	3
H1-C3-OH-HO	0.167	0	3
H1-C3-C3-HC	0.156	0	3

Table 3.7D. Lennard-Jones parameters for the IPA force field.

Atom	Epsilon (kcal mol <sup>-1</sup> )	Sigma (Å)
H1	0.0157	1.2357
HC	0.0157	1.3248
C3	0.1094	1.6998
OH	0.2104	1.5332
HO	0	0



# CHAPTER 4

## Results and Discussion

### 4.1 Ab Initio Results

A comparison of the atomic partial charges calculated in this study for the DMOF-1 ligands (BDC and DABCO) is reported in Tables 4.1 and 4.2. From the tables it can be immediately seen that the overall differences among charges derived using MP2 perturbation theory and DFT functionals (B3LYP and M062X) are small for both ligands. For BDC, the charge on the C2 atom varies the most among methods. The difference in the charges calculated using the isolated BDC and the BDC-cluster are also small. Unlike the BDC ligand, large charge differences were found between the charges obtained for the isolated DABCO and the DABCO-cluster. For the isolated DABCO, the N atoms have negative charges, whereas the DABCO-cluster has positive N atoms, which can be attributed to the different bonding configurations. In the DABCO-cluster, Zn is a Lewis acid that bonds weakly with the N lone pair. From Table 4.2 it can be seen that changes of the Zn-N bond length does not significantly affect the DABCO charges. When using the cluster representation of each DMOF-1 ligand, the Zn charges were chosen to neutralize the unit cell ( $Zn_2(BDC)_2(DABCO)$ ).

Table 4.1. BDC ligand charges from different ab initio methods.

Atom (model)	B3LYP (e <sup>-</sup> )	M062X (e <sup>-</sup> )	MP2 (e <sup>-</sup> )
O (Isolated)	-0.714	-0.729	-0.707
C2 (Isolated)	0.626	0.6465	0.502
CA1 (Isolated)	-0.031	-0.028	-0.012
CA2 (Isolated)	-0.115	-0.134	-0.133
HA (Isolated)	0.032	0.054	0.045
O (Cluster)	-0.727	-0.744	-0.713
C2 (Cluster)	0.707	0.720	0.647
CA1 (Cluster)	0.012	0.007	0.074
CA2 (Cluster)	-0.095	-0.111	-0.13
HA (Cluster)	0.102	0.119	0.114

Table 4.2. DABCO ligand charges from different ab initio methods. Isolated DABCO ligands do not have Zn–N distances, which are labeled n/a.

Atom (model, Zn–N distance)	B3LYP	M062X	MP2
N3 (Isolated, n/a)	-0.4895	-0.496	-0.516
C3 (Isolated, n/a)	0.167	0.1363	0.165
H1 (Isolated, n/a)	-0.002	0.0135	0.0035
N3 (Cluster, 2.074)	0.1575	0.1205	0.1705
C3 (Cluster, 2.074)	0.0075	-0.0278	-0.0177
H1 (Cluster, 2.074)	0.027	0.0407	0.0312
N3 (Cluster, 2.400)	0.139	0.0740	0.15
C3 (Cluster, 2.400)	0.007833	-0.0062	-0.0003
H1 (Cluster, 2.400)	0.01575	0.0317	0.0195

Our analysis indicates that the M062X functional is more effective than B3LYP for the BDC–cluster optimization. Table 4.3 compares the Zn–O bond, Zn–Zn distance, and Zn–O–C angle for the optimizations performed with and without the LAN2DZ basis set. As shown in the table, the M062X functional with the effective core potential promises the most accurate results. The M062X functional was marginally worse than B3LYP at reproducing the correct Zn–O distance but performs better at reproducing the correct Zn–Zn distance and Zn–O–C angle. Interestingly, the B3LYP functional with

the LAN2DZ ECP basis set reproduces the Zn–Zn distance and the Zn–O–C angle better than B3LYP without ECP but is less accurate at reproducing the Zn–O bond distance.

*Table 4.3.* BDC–cluster optimizations with different ab initio methods and basis sets. Use of the LAN2DZ ECP basis set is indicated next to the functional where appropriate. The crystal structure data is in parentheses.

DFT functional (ECP)	Zn–O (2.027 Å)	% Error	Zn–Zn (2.884 Å)	% Error	Zn–O–C (125.54°)	% Error
M062X	2.02	0.44	2.75	4.74	124.54	0.80
M062X (ECP)	2.026	0.03	2.816	2.36	125.58	0.03
B3LYP	2.023	0.18	2.681	7.06	123.45	1.66
B3LYP (ECP)	2.039	0.59	2.796	3.06	125.14	0.32

The Zn–O and Zn–N bond constants were fit to harmonic potentials with force constants of 280 kcal mol<sup>-1</sup> and 140 kcal mol<sup>-1</sup>, respectively. The results of the fitting procedures are shown in Figure 4.1. When comparing these values to the C3-HC (GAFF database atom notation) bond constant of 674.6 kcal mol<sup>-1</sup>, the relative Zn–ligand bond weakness is evident. These weak bond constants are likely a driving factor in the hydro-instability of DMOF-1 and help explain the reversible DABCO loss with humidity without loss of slightly stronger Zn–O bonds.<sup>76</sup>

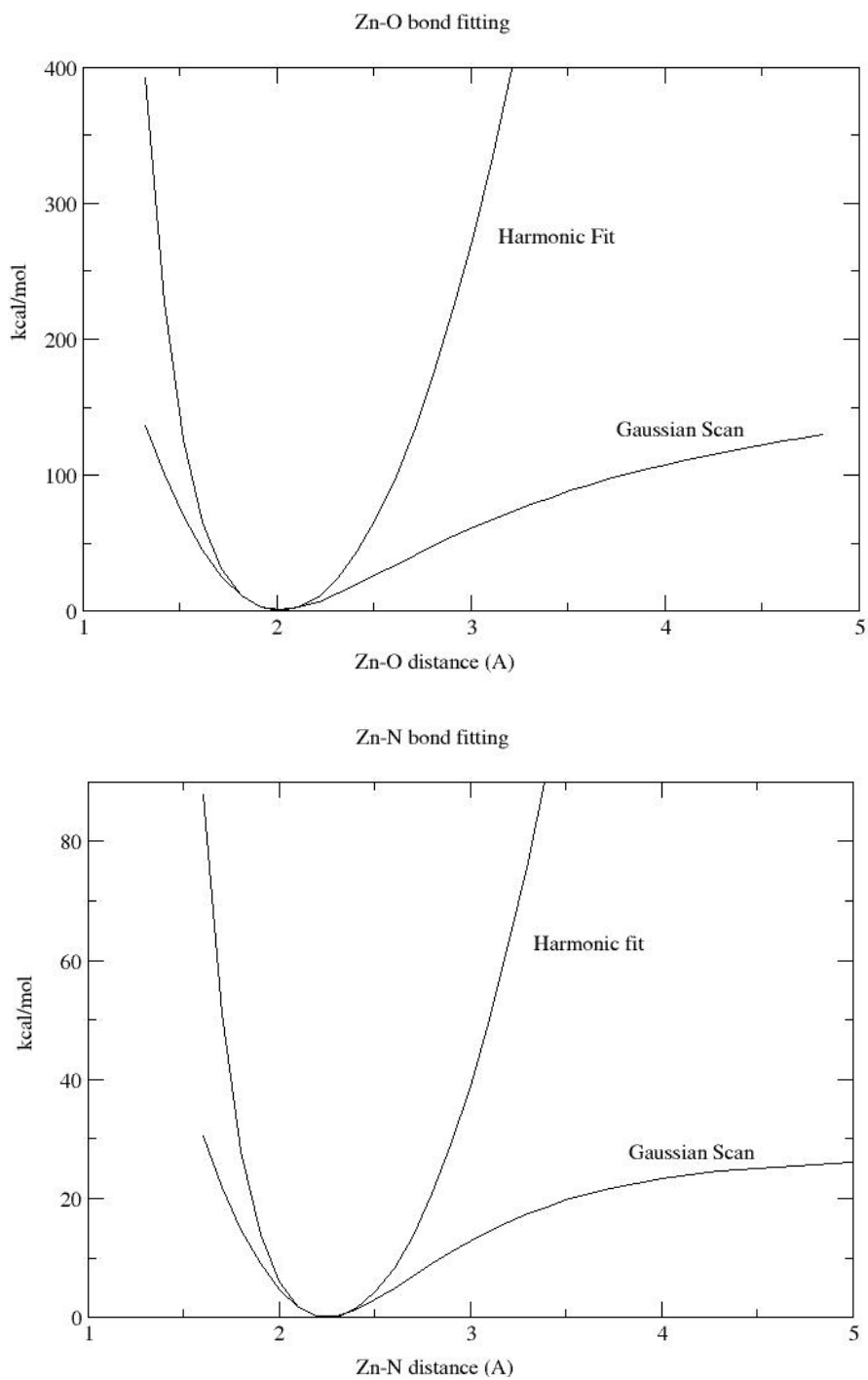


Figure 4.1. Harmonic fitting to Zn-O (top) and Zn-N (bottom) scans at the MP2 level of theory.

### 4.1.1 Post-Synthetic Modification

The isolated BDC-AM1 to BDC-AM3 optimized structures are found to have distinct hydrogen bonds between the amine chain and nearest carbonyl oxygen. The hydrogen bonded position is not the most favorable for the BDC-AM4 chains in the B3LYP and MP2 optimizations, although it corresponds to the most stable configuration in the M062X optimization. For the structures of BDC-AM5 and longer chains, the hydrogen bonded position is never the most favorable independently of the ab initio methods employed. It is interesting to note that in the hydrogen bonded configuration, the amine chain orientation remains close to the plane of the BDC, while in the other cases, it points perpendicularly to it. The presence of the amide chains in the framework also affects the charges of the benzene rings. In particular, the carbon that is directly bonded to the amide chain has a large positive charge relative to the negative carbons on the benzene ring. The symmetry of the atom types in the modified BDC ligands is broken by the presence of the amide chain resulting in a more complicated labeling scheme, which has been described in Figure 3.5.

The partial optimizations of the amine chain, which were performed by fixing the attached BDC and metal clusters at the M062X optimized configurations, show that the most effective position for BDC-AM1-cluster to BDC-AM4-cluster is in the hydrogen bonded position with the ligand oriented towards a Zn cluster. Amine chains longer than AM4 are too long to be effectively optimized within a cluster model. This can be ascribed to the fact that these chains are long enough to interact with the Zn cluster, resulting in a noticeable charge transfer between the alkyl chain and the Zn

atoms. For ease of computation, an isolated amine chain model was used for the atomic partial charges for all the amine chains longer than AM1. As described in the previous chapter, in this model the framework charges were all taken from the BDC-AM1-cluster, while the alkyl chain charges were obtained from calculations for the isolated amine chains performed at the MP2 level of theory. The partial charges for AM1 to AM4 are listed in Tables 3.4 and 3.5 along with the other force field parameters.

## **4.2 Non-Bonded Type Force Fields**

### **4.2.1 Non-Bonded Force Field**

In this study, no model relying on the electrostatic interactions to represent the Zn–ligand bonds satisfactorily reproduces DMOF-1, DMOF-1+2BEN or any post-synthetically modified DMOF-1. This can be attributed to the overestimation of the Zn–ligand flexibility as well as to the presence of the paddlewheel Zn–cluster that places many highly charged atoms in close proximity. As a consequence, non-bonded force fields highly depend on the Zn partial charge and van der Waals radius. In Table 4.4, the effects of using charges derived from the isolated BDC and BDC–cluster models on the DMOF-1 unit cell vectors are summarized. The results of varying the Zn characteristic radius and results of the DMOF-1+2BEN simulations are also included. Table 4.5 compares the error from the experimental Zn–Zn distance, Zn–N bond length, and Zn–O bond length to the simulated DMOF-1 values.

Table 4.4. Comparison between original M062X charges and the BDC-cluster using MP2-theory with LAN2DZ basis set charges with Zn radius at 1.1 Å and 1.4 Å. The length of axes are in Å.

System	Theory	Zn radius (Å)	Axis <i>a</i>	% error	Axis <i>b</i>	% error	Axis <i>c</i>	% error
DMOF	M062X	1.1	10.6218	2.80	10.6218	2.81	9.6700	0.64
DMOF	M062X	1.4	11.4581	4.84	11.4581	4.84	10.0977	5.09
DMOF	MP2	1.1	10.7445	1.68	10.7445	1.69	9.6885	0.83
DMOF	MP2	1.4	10.9322	0.03	10.9322	0.03	10.1055	5.17
2BEN	MP2	1.4	19.1475	12.2	8.8890	34.2	10.0115	3.52

Table 4.5. Percent error of simulated DMOF-1 Zn-distances relative to crystal data.

Charges	Zn radius (Å)	Zn–Zn dist. (Å)	% error	Zn–N dist. (Å)	% error	Zn–O dist. (Å)	% error
M062X	1.1	3.0190	4.68	2.0213	2.54	1.7953	11.26
M062X	1.4	3.1839	10.40	2.1661	4.44	1.9231	4.94
MP2	1.1	2.8868	0.09	2.0868	0.62	1.8667	7.72
MP2	1.4	3.0186	4.67	2.2385	7.93	2.0065	0.82

When using a Zn van der Waals radius of 1.1 Å, the BDC-cluster model better reproduces the DMOF-1 unit cell vectors than the isolated BDC model. The BDC-cluster model also closely reproduces the *c* axis, the Zn–Zn distance, and the Zn–N bond, but underestimates the Zn–O bond by 0.17 Å. In order to better reproduce the Zn–O distance, the van der Waals radius of Zn was raised from 1.1 Å to 1.4 Å. However, this modification it also increased the Zn–N and Zn–Zn distances. Systematically large Zn–Zn distances are caused by the Zn–Zn repulsions, which are partially reduced by the Zn–N attractions. This affects the isolated model by increasing the *a* and *b* axes from 10.6218 Å to 11.4581 Å, and the *c* axis from 9.6700 Å to 10.0977 Å, significantly decreasing the overall accuracy of the model. In this context, the BDC-cluster model is less affected because of the relatively smaller Zn charges. In this case, the *a* and *b* axes increased from 10.7445 to 10.9322 Å, and the *c* axis from 9.6885 Å to

10.1055 Å. Since the BDC-cluster model with 1.4 Å Zn radius best represent the BDC-Zn interactions, it was chosen to model the breathing motion of the DMOF-1+2BEN system.

The breathing motion of DMOF-1 occurs in the plane of the BDC ligands. Therefore, it is believed that the Zn-BDC interactions are more important than the Zn-DABCO interactions. Unfortunately, the breathing simulation of DMOF-1+2BEN resulted in an almost flattened NP configuration, caused by a too large framework flexibility. The simulated structure is narrower than the correct crystal structure by 4.6114 Å, or 34.2 % relative to the *a* axis. This shows that an accurately modeled Zn-O bond length does not necessarily translate into an accurate representation of the bond directionality.

The simulations with DMOF-1-AM1, like those with DMOF-1+2BEN, also suffered from excess flexibility. The system folded into a non-physical configuration that maximizes the chain-chain interactions, shown in Figure 4.2. This folding takes place by the flattening and maneuvering of chains from some pores, which crowd the chains into the remaining open pores. As for the DMOF-1+2BEN system, the excess flexibility in DMOF-1-AM1 is the result of Zn-O bonds that are not directional and allow unphysical orientations. The lack of directionality in Zn-O bonds is inherent in the non-bonded model, and as such does not represent the DMOF-1 framework flexibility effectively. These drawbacks are overcome in the restrained force field, in which Zn-O bonds are oriented and the DMOF-1 framework flexibility, restrained, through addition of Zn-O-C-C dihedrals.



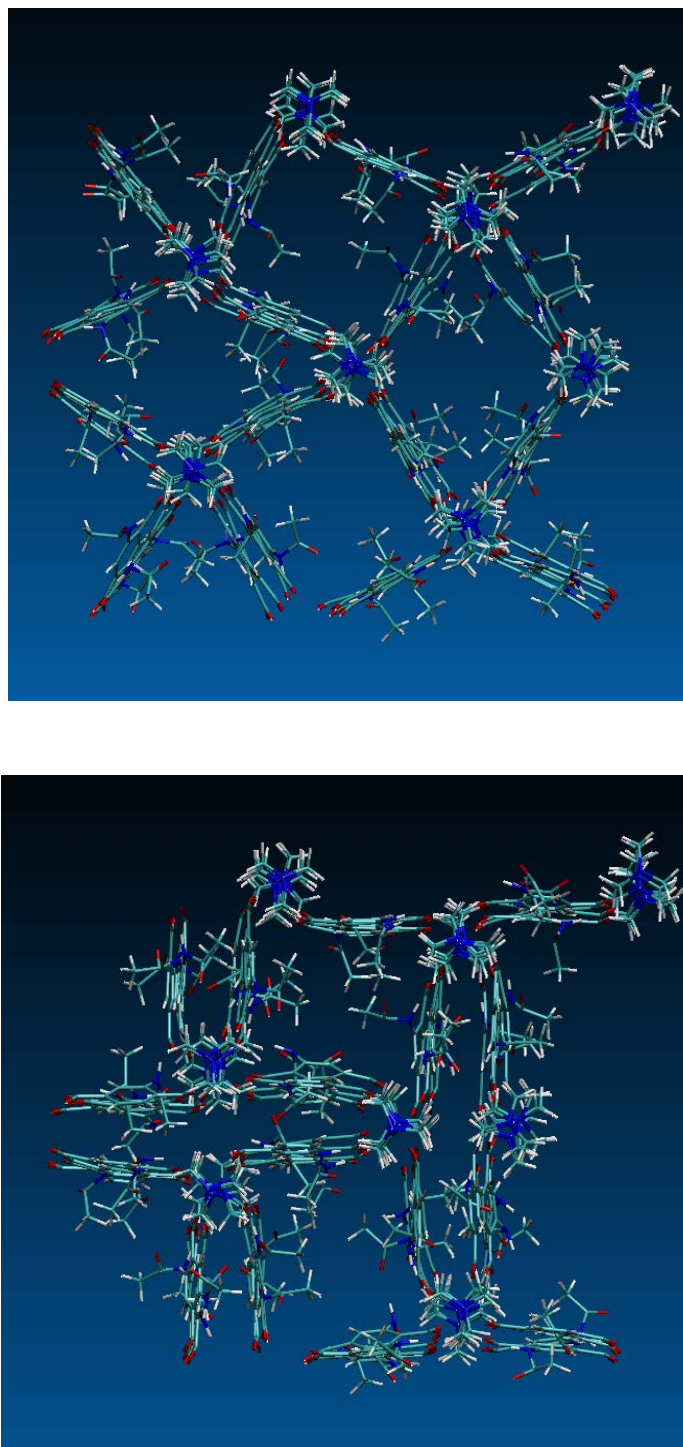


*Figure 4.2.* DMOF-1-AM1 intermediary configuration (*top*) and final configuration (*bottom*).

### 4.2.2 Restrained Force Field

The restrained force field incorporated harmonic potentials into the non-bonded force field and resulted in significantly improved simulations of the DMOF-1 framework flexibility. To accomplish this, Zn–O–C angles and Zn–O–C–C dihedrals were added as harmonic potentials to reduce framework flexibility by giving the Zn–O bonds directionality. Zn–O–C angles were used to prevent the BDC “slipping” motion that orients a carboxyl oxygen atom between two Zn atoms to maximize the Zn···O electrostatic interactions. Zn–O–C–C dihedrals were used to prevent the extreme flexibility previously seen with the non-bonded force field. As with MIL-53, the Zn–O–C–C dihedral was found to be fundamental to the DMOF-1 breathing motion. The harmonic potentials for Zn–O–C angles and Zn–O–C–C dihedrals were set to  $31.664 \text{ kcal mol}^{-1} \text{ rad}^{-2}$  at  $111.12^\circ$  and to  $3.337 \text{ kcal mol}^{-1} \text{ rad}^{-2}$  at  $180^\circ$ , respectively.

The addition of Zn–O–C angles and Zn–O–C–C dihedrals in the restrained force field resulted in the same accuracy of DMOF-1 simulations as the non-bonded force field (results in Table 4.4), and resulted in more accurate DMOF-1+2BEN simulations. The restrained force field simulations of DMOF-1+2BEN resulted in a, b, and c unit cell vectors of  $17.0665 \text{ \AA}$ ,  $13.573 \text{ \AA}$ , and  $10.088 \text{ \AA}$ , respectively. These values are highly accurate being only 0.39%, 0.54%, and 3.68% larger than the corresponding experimental values ( $17.000 \text{ \AA}$ ,  $13.500 \text{ \AA}$ , and  $9.730 \text{ \AA}$ ).

However, the DMOF-1+2BEN simulations were found to be erratic with the structure often spending several hundred picoseconds in the LP and NP configurations,

which was sometimes accompanied by rapid changes between the LP and NP. The correct average values were obtained over the course of the 4 ns simulation. Because of the erratic simulations, the benzene molecules were found to be randomly oriented and unable to maintain the correct T-shape configurations seen in the crystal structure data (Figure 2.1). The inability of benzene molecules to maintain the correct configurations indicates that the physics behind DMOF-1 breathing is not correctly simulated, even though the simulations reproduced the experimental values.

The erratic behavior of the system prevents the benzene molecules from maintaining stable positions and is attributed to the highly charged metal cluster having large fluctuations of the Zn atomic positions. Essentially, the Zn atoms strongly repel each other within a small attractive cage, defined by the negatively charged O and N atoms. In DMOF-1, the Zn atoms are able to maintain stable positions, but in DMOF-1+2BEN the Zn are perturbed by the change of the Zn–O–C–C dihedral through the BDC···benzene interactions. The initial Zn perturbation, in combination with the strong repulsions and attractions with each other and the other ligands, result in large random fluctuations of the Zn positions, which, in turn gives rise to the erratic behavior of the Zn–O–C–C dihedrals. The large fluctuations of Zn–O–C–C dihedrals directly translate into large breathing fluctuations. With Zn–O–C–C force constants larger than  $3.44 \text{ kcal mol}^{-1} \text{ rad}^{-2}$  the benzene molecules are unable to perturb the framework, which remains in the open pore indefinitely.

Using a Zn–O–C–C force constant of  $3.37 \text{ kcal mol}^{-1} \text{ rad}^{-2}$  it was possible to obtain the correct DMOF-1+2BEN unit cell vectors. However, this value was found to be too stiff for all post-synthetically modified DMOF-1, which remained the LP

configuration indefinitely. By reducing the Zn–O–C–C dihedral to  $2.50 \text{ kcal mol}^{-1} \text{ rad}^{-2}$  the structure reduced into the NP configuration for the whole DMOF-1-AM series. With this value of the force constant for the Zn–O–C–C dihedral angles DMOF-1+2BEN folds into a flattened NP configuration. Although the correct NP/LP structures were not obtained with the restrained force field, the Zn–O–C–C dihedral prevented the previously seen non-physical configurations (Figure 4.2) that resulted from the unphysical bending of the non-directional Zn–O bonds. No intermediate values were found for the force constant of the Zn–O–C–C dihedral angles that provide a correct description of both DMOF-1 upon post-synthetic modification and DMOF-1+2BEN.

The difficulties in modeling both post-synthetically modified DMOF-1 and DMOF-1+2BEN highlight the problem of using electrostatic interactions to approximate the Zn–ligand bonds. The large number of strongly interacting atoms within the Zn cluster prevents all unit cell vectors from being correctly modeled at the same time in DMOF-1 simulations. Another consequence of the strong electrostatic interactions is the erratic behavior observed in the simulations of DMOF-1+2BEN with the restrained force field. Because this behavior is directly connected to the use of electrostatic Zn–ligand bonds, it was determined that a fully-bonded force field would better represent both DMOF-1 and the correct physics behind the DMOF-1 breathing.

### 4.3 Fully-Bonded Type Force Field

The DL\_POLY\_4 MD package was chosen for ease in specifying a fully-bonded force field with bonds that go through the periodic boundaries, as well as for the

availability of a fully anisotropic NPT ensemble. The fully-bonded force field has less attractive and repulsive forces within the Zn clusters, which is the fundamental weakness of the non-bonded type of force fields discussed above. As a consequence, it was found that the fully-bonded model is more successful than the non-bonded types of force fields in reproducing both DMOF-1 and DMOF-1+2BEN unit cell vectors. The correct type of physics was also observed in the DMOF-1+2BEN simulations. DMOF-1+1IPA to DMOF-1+4IPA was simulated and found to qualitatively reproduce the correct breathing behavior. However, DMOF-1-AM1 to DMOF-1-AM4 was poorly modeled. For the investigation of DMOF-1 flexibility with benzene, with IPA, and with post-synthetic modifications, it is useful to consider the unit cell vectors along the axes of the breathing motion as illustrated in Figure 4.3.

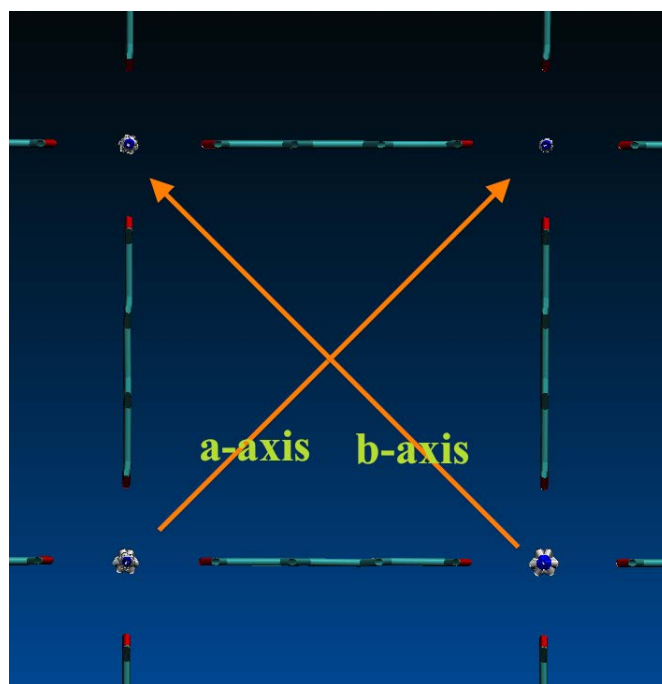


*Figure 4.3.* Taking the unit cell axes along the direction of breathing is useful for comparison.

Table 4.6 summarizes the results of the simulations with DMOF-1, DMOF-1+1.5–2BEN, and DMOF-1+2–3IPA. DMOF-1-1.25BEN, DMOF-1-1IPA, and DMOF-1+4IPA were not found to breathe and, therefore, are not included in the table. It can be seen from the table that all the DMOF-1 unit cell vectors can be reproduced simultaneously, a major advantage of the fully-bonded force field over the non-bonded force field. The calculated DMOF-1 unit cell vectors are within 0.5% and 5% of the crystal data for the fully-bonded and non-bonded force fields, respectively. The percent error from the correct Zn–Zn distance, Zn–N bond, and Zn–O bond in DMOF-1 is 2.93% , 2.15%, and 0.78%. The increase in accuracy of the fully-bonded force field results from reduced electrostatic repulsion within the Zn cluster.

*Table 4.6.* Results of DMOF-1 and DMOF-1 with varying amounts of benzene and IPA per unit cell. For systems with no experimental data the percent Error is listed as n/a. The length of axes are in Å.

System	Axis <i>a</i>	% Error	Axis <i>b</i>	% Error	Axis <i>c</i>	% Error
DMOF	10.9593	0.2791	10.9593	0.2791	9.6740	0.0262
1.5 BEN	17.3433	n/a	13.2473	n/a	9.6419	n/a
1.75 BEN	17.7107	n/a	12.7242	n/a	9.6379	n/a
2 BEN	17.3803	1.8390	13.1361	2.6984	9.6578	0.1421
2 IPA	18.6617	n/a	21.5313	n/a	9.6424	n/a
3 IPA	18.6727	15.8930	10.6842	11.2904	9.6418	3.4977

The decrease of large electrostatic contributions is the result of the increase in the number of bonds, angles, and dihedrals that represent the Zn–ligand interactions. Within a force field description, atoms that are involved in a bond, angle, or dihedral do not interact electrostatically. These “bonded” interactions are entirely described by

their potential function representations and do not include any non-bonded forces, except the dihedrals that may include some contribution from the van der Waals interactions. In addition to Zn–ligand bonds, angles, and dihedrals the correct representation of the Zn cluster required the use of a Zn–Zn bond.

Using only Zn–ligand bonded interactions initially resulted in a poor model of the DMOF-1 framework because of the large Zn $\cdots$ Zn electrostatic repulsions. The strong repulsions were eliminated by the creation of the Zn–Zn bond. It must be noted that the Zn–Zn bond does not exist in reality, but is used in the simulations strictly for the purpose of eliminating the Zn $\cdots$ Zn electrostatic repulsion. It was shown that fictitious metal-metal bonds in paddle-wheel containing MOFs, such as DMOF-1, are required to accurately reproduce the metal clusters. The first flexible force field for the paddle-wheel MOF Cu-BDC (HKURST-1) required a fictitious Cu-Cu bond to prevent the close metals from repelling each other.<sup>77</sup> The metal-metal bond compensates for using a simple point charge model, in which explicit bonds, angles, and dihedrals do not interact electrostatically. The removal of the Zn $\cdots$ Zn repulsions through the use of the Zn–Zn bond resulted in an improved stability of DMOF-1+2BEN. The benzene molecules were able to stabilize in the DMOF-1 pore windows, instead of being randomly distributed as it was with the restrained force field. The DMOF-1+2BEN structure oscillates between the correct NP structure and a slightly smaller NP structure depending upon the benzene orientation. The combination of benzene orientations results in *a* and *b* axes that are slightly too long and short, respectively, and an overall cell shape slightly narrower than that obtained from the experimental crystal data. Figure 4.4 shows a plot of the unit cell parameters over time.

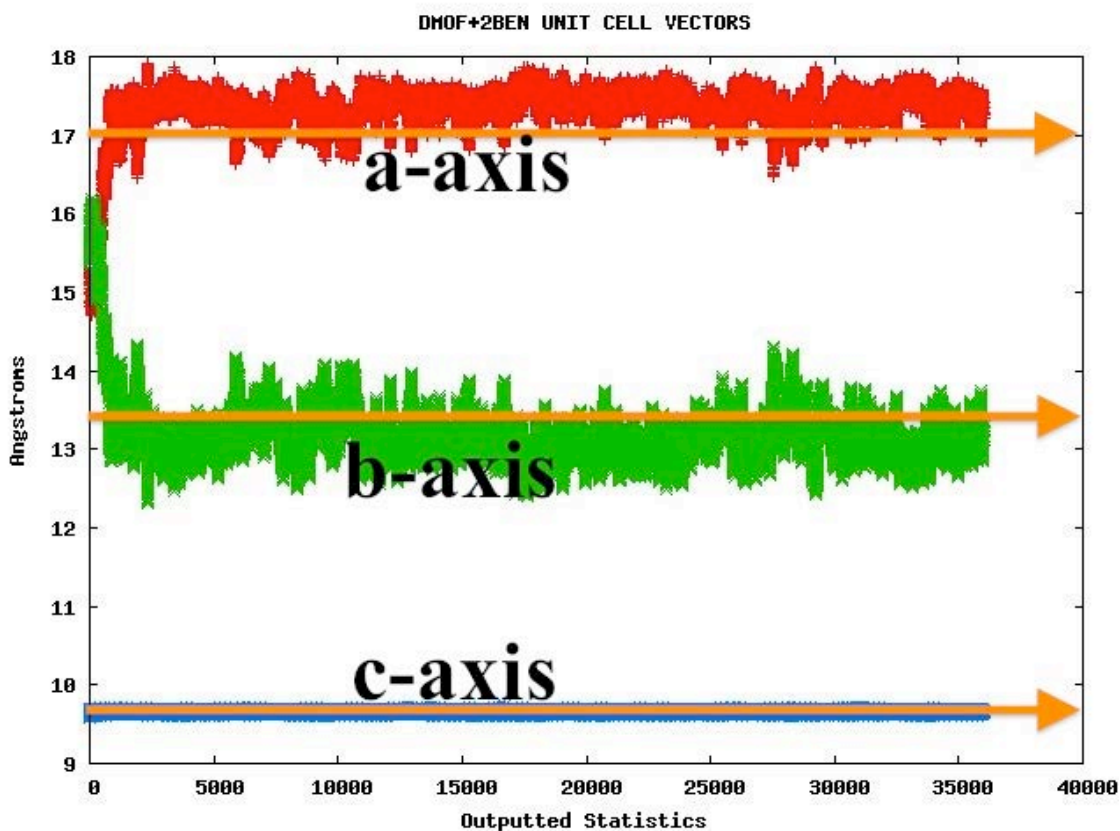
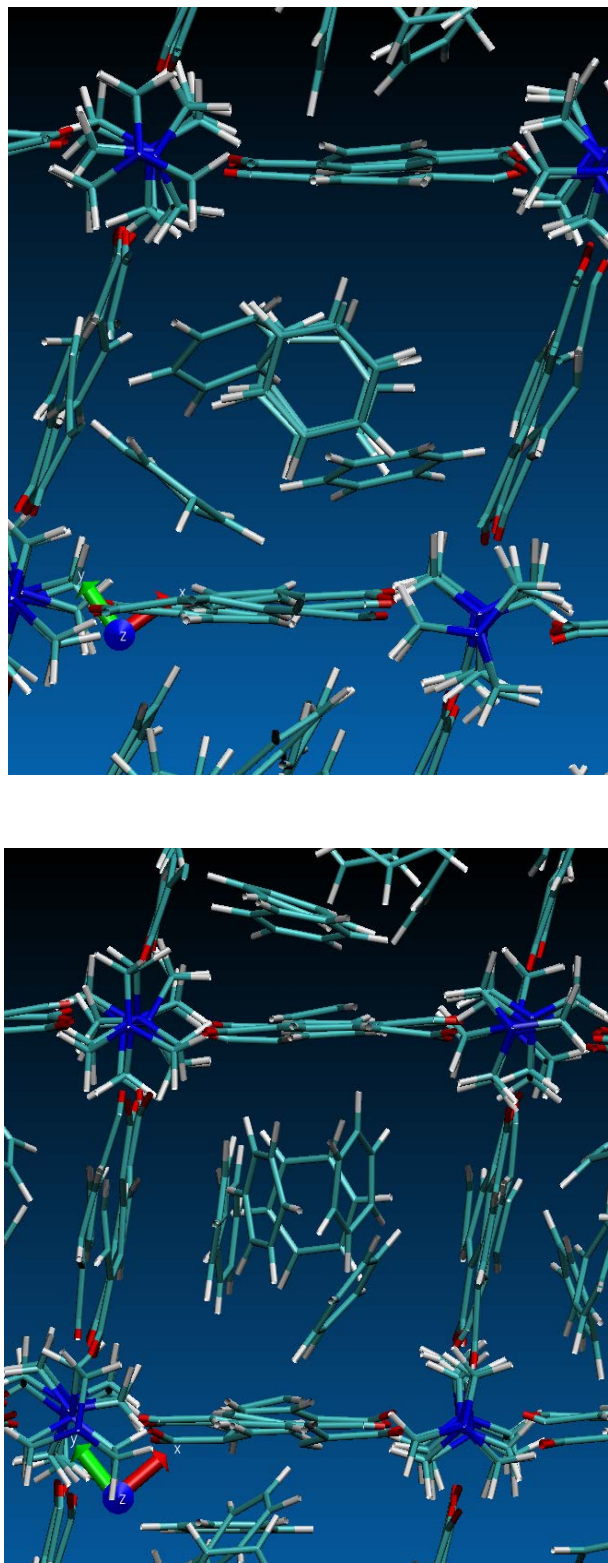


Figure 4.4. DMOF-1+2BEN unit cell vectors during a 7.5 ns simulation. Statistics were outputted every 200 steps with a 1 fs time step. The correct unit cell parameters are marked with arrows.

The T-shape orientation of the benzene molecules results in the correct cell shape while other configurations for the benzene in the pore window, such as parallel to the BDC ligands, cause the structure to be too narrow. The benzene molecules in the T-shape and parallel orientations for the benzene molecules in the window faces are shown in Figure 4.5.





*Figure 4.5.* Snapshots of the DMOF-1+2BEN simulation. Benzene in correct T-shape configuration (left) and parallel configuration (right).

The localized benzene molecules in the pore windows indicate that the correct physics of the DMOF-1 breathing with benzene is correctly reproduced. The number of benzene molecules necessary to simulate the breathing motion in DMOF-1 is 1.5 benzene per unit cell. In principle 1 benzene per unit cell is required, which gives one benzene molecule per pore window. The simulations with 1 to 1.25 benzene molecules per unit cell were unable to maintain the required positions within the pore windows to initiate breathing. In DMOF-1+1.5BEN to DMOF-1+2BEN simulations, the benzene molecules that induce breathing are maintained in place through steric interactions with other nearby benzene molecules, usually localized near the DABCO (Figure 4.4 (*left*)). Benzene molecules localized near the DABCO ligands are also seen in the experimental crystal data, which indicates the correct physics behind the DMOF-1 framework and benzene molecules are correctly reproduced.

After the successful simulation of DMOF-1+2BEN, the DMOF-1+IPA simulations were simulated to test the force field transferability from one adsorbate to another. The DMOF-1 breathing with IPA qualitatively reproduced the correct behavior. DMOF-1+IPA initiates the LP-NP transition at 2 IPA per unit cell, earlier than experimental value of 3, but reopens into the LP with 4 IPA per unit cell. DMOF-1+3IPA simulations resulted in a qualitative reproduction of the correct NP configuration, with the  $a$  and  $b$  axes being 16% longer and 11% shorter, respectively, than the experimental data. The IPA gather in pore centers, interacting with each other instead of the framework. The LP-NP transition is induced by IPA-IPA interactions between cells, pulling themselves closer together. With 4 or more IPA molecules per

unit cell the simulated structure opens into the LP configuration due to steric interactions with the framework.

The experimental data indicate that the IPA molecules in the reopened LP configuration should form well-ordered hydrogen bonded dimers through the spaces within the BDC grid (Figure 2.3). Because the hydrogen bonding between pores was not observed in the simulations and the IPA molecules tend to interact with each other over the framework, it is likely that the IPA force field used is not realistically represented within the DMOF-1 framework. Even though the IPA interactions with DMOF-1 were not entirely correct, the qualitative reproduction of the DMOF-1 breathing with respect to the number of IPA molecules and unit cell vectors. The successful modeling of DMOF-1+2BEN and DMOF-1+3IPA with the fully-bonded force field indicates the force field transferability for adsorbate-induced breathing.

The modeling of the correct NP and LP configurations of post-synthetically modified DMOF-1 was less successful than the modeling the NP and LP configurations of DMOF-1+IPA. The fully-bonded force field correctly simulated DMOF-1-AM3 as the NP configuration and DMOF-1-AM4 as LP, but incorrectly simulated DMOF-1-AM1 and DMOF-1-AM2 as the LP configurations. Nevertheless, this is an improvement over the restrained force field that incorrectly simulates all DMOF-1-AM $n$  as the LP configuration. Table 4.7 summarizes the length of the unit cell vectors of DMOF-1-AM1 to DMOF-1-AM4. The table shows a sudden transition from the LP to the NP structure between DMOF-1-AM2 to DMOF-1-AM3 that partially opens into the LP again with DMOF-1-AM4.

*Table 4.7.* DMOF-1-AM1 to DMOF-1-AM4 unit cell vectors. The length of axes are in Å.

PSM	a-axis	b-axis	c-axis
AM1	15.5224	15.6060	9.6832
AM2	15.7958	15.2961	9.6503
AM3	17.0869	13.7434	9.6588
AM4	16.4147	14.5291	9.6419

The DMOF-1-AM1 and DMOF-1-AM2 results are counter to the experimentally determined NP configurations. It is likely that in the fully-bonded force field, the AM1 and AM2 chains are too short for effective interaction. The longer AM3 chains confirm this because the DMOF-1-AM3 simulations were found to induce the LP/NP transition. The AM4 chains are also long enough to interact, with the framework in which leads to an intermediate LP structure due to the competing attractive and steric effects. Because the experimental isotherms of adsorption indicate NP structures for DMOF-1-AM1 and DMOF-1-AM2, it is possible that the addition of adsorbates, such as CO<sub>2</sub>, could bridge the gap between amine chains and induce the transition to the NP structure in the simulations.

The inability of the AM1 and AM2 chains to induce DMOF-1 breathing could also be the result of insufficient chain-chain interactions. Because the chain length induces breathing from AM2 to AM3 without a significant difference of the alkyl chain charges, the inability to reproduce the NP configuration with AM2 may be the consequence of inaccurate representation of the van der Waals parameters. The attachment of the amine chains directly to the framework may also make the simulations of the breathing motion more difficult relative to the mobile adsorbates. The adsorbate induced breathing may be better represented because the DMOF-1

framework was specifically tuned to reproduce breathing with benzene. The success at modeling DMOF-1 with adsorbates and the failure to model the DMOF-1-AM $n$  series highlights that the fully-bonded force field is not transferable to post-synthetically modified systems.

The issue of force field transferability between adsorbates and post-synthetic modifications was not resolved during this study. It is difficult to determine why breathing is seen with DMOF-1+BEN and DMOF-1+IPA but not with DMOF-1-AM1 and DMOF-1-AM2. The DMOF-1+IPA results suggest that the framework is too flexible, or that the Zn–O–C–C dihedral is too weak, as indicated by the too small NP configuration. Contrary, the DMOF-1-AM1 and DMOF-1-AM2 resulted in LP configurations, indicating that the framework is too stiff, or that the Zn–O–C–C dihedral is too strong. These apparently contradicting may indicate that other DMOF-1 framework force field parameters may need some refinement to reproduce the breathing behavior in more complex systems.

Although the transferability issues were not resolved, it is demonstrated that the fully-bonded force field provides a significantly more accurate representation of the DMOF-1 framework than the non-bonded type force fields. The fully-bonded force field more accurately reproduces DMOF-1, DMOF-1+2BEN, the DMOF-1-AM $n$  series, and qualitatively reproduces DMOF-1+3IPA.

## CHAPTER 5

### CONCLUSION

This study created the first fully flexible force field to investigate the breathing motion of DMOF-1. During the study, three fully flexible force fields were created: the non-bonded force field, the restrained force field, and the fully-bonded force field. Both the non-bonded and restrained force fields use electrostatic interactions to model the Zn–ligand bonds, while the fully-bonded force field explicitly describes the Zn–ligand bonds, angles, and dihedrals. The two non-bonded type force fields did not adequately simulate DMOF-1, DMOF-1+2BEN, nor any of the simulations of the DMOF-1-AM $n$  series. The fully-bonded force field successfully modeled DMOF-1, DMOF-1+2BEN, and DMOF-1+3IPA, but did not adequately model all structures of the DMOF-1-AM $n$  series.

The process of creating the force fields involved a detailed study of the DMOF-1 framework using DFT and MP2 ab initio methods. The framework ligands were represented using isolated models and cluster models that connect the isolated ligand between two Zn clusters. It was found that the M062X DFT functional promises more accurate optimized structures for the BDC–cluster than the B3LYP DFT functional. This was also found using the LAN2DZ ECP basis set for the Zn atoms. The partial charges for both ligand representations were calculated using each level of theory with the CHELP method using a 1.0 Å Zn radius. The differences between the DFT

functionals (B3LYP and M062X) and MP2 are small, indicating that the less computationally expensive DFT methods are suitable for obtaining accurate partial charges.

The non-bonded force field could not simultaneously reproduce all axes of DMOF-1 at the same time because of the strong repulsive interactions within the Zn cluster. As a result, using charges from the BDC-cluster that have reduced Zn charges improved the accuracy in reproducing the DMOF-1 simulations. The Zn van der Waals radius was increased from 1.1 Å to 1.4 Å to reproduce the correct Zn–O bond length. The non-bonded force field utterly failed to accurately simulate DMOF-1+2BEN and DMOF-AM1, which resulted in highly unphysical orientations for both. The extremely flexible framework was determined to be a consequence of Zn–O bonds that were not directional. Thus, harmonic potentials were used in the restrained force field to help orient the Zn–O bonds.

In the restrained force field, harmonic potentials were used to add Zn–O–C angles and Zn–O–C–C dihedrals to the non-bonded force field. These additional parameters reduced the framework flexibility by preventing the Zn–O bond from bending into unphysical orientations. The restrained force field accurately reproduces the correct DMOF-1+2BEN unit cell vectors but predicts all DMOF-1-AM $n$  to be in the LP configuration. While the correct DMOF-1+2BEN unit cell vectors are correctly reproduced, the LP/NP transition in simulation was found to be erratic and the correct positions of the benzene molecules in the framework could not be reproduced. The Zn atom positions randomly changed after being perturbed by the BDC $\cdots$ benzene interactions, which caused the Zn–O–C–C dihedral angle to fluctuate randomly.

The fully-bonded force field used Zn–ligand bonds, angles, and dihedrals to reduce the amount of repulsive charges within the Zn clusters. In turn, this removed the erratic behavior of the Zn–O–C–C dihedral and resulted in improved modeling of the DMOF-1 breathing. The fully-bonded force field is capable of accurately modeling DMOF-1 and DMOF-1+2BEN, and qualitatively modeling breathing with DMOF-1+3IPA. However, the DMOF-1-AM $n$  series could not be correctly modeled, however. The inability to model the post-synthetically modified DMOF-1 is thought to be a consequence of poor force field transferability.

Issues with force field transferability are not new. Flexible force fields for MIL-53 have required the adjustment of both van der Waals parameters of the framework and of the Zn–O–C–C dihedral angle to reproduce the breathing behavior for specific adsorbents. The reproduction of the breathing motion of MIL-53 with CO<sub>2</sub> and H<sub>2</sub>S required significantly different van der Waals parameters of the framework. In my opinion, the Lennard-Jones parameters derived from common force fields are not suitable for accurate use in MOFs and are a primary cause of force field transferability difficulties. The sets of Lennard-Jones parameters used in common force fields are usually designed for purely organic systems, not heterogeneous confined spaces such as MOFs. The adjustment of Lennard-Jones values and other force field parameters tends to cause force fields to specialize and be able to reproduce effects of only one adsorbate at a time.

Future studies into flexible force fields for breathing MOFs must resolve the force field transferability problem. Currently the fully-bonded type of force fields are the only type that can correctly reproduce MOF breathing, but usually the parameters



for the metal-ligand interactions have not been studied experimentally. As more experimental data is gathered, in particular more spectroscopic data in particular, the force constants for bonds, angles, and dihedral angles around the metal coordination centers can be determined, which will help the parameterization of accurate force fields for MOF materials.

## REFERENCES

- (1) O'Keeffe, M. *Chem Soc Rev* **2009**, *38*, 1215.
- (2) Maddox, J. *Nature* **1988**, 335.
- (3) MacGillivray, L. R. *Metal-Organic Frameworks*; John Wiley & Sons: New Jersey, 2010.
- (4) Li, H.; Eddaoudi, M.; Groy, T. L.; Yaghi, O. M. *J Am Chem Soc* **1998**, *120*, 8571.
- (5) Yaghi, O.; O'Keeffe, M.; Reineke, T. M.; Chen, B.; Li, H.; Moler, D. B.; Eddaoudi, M. *Accounts Chem Res* **2001**, *34*, 319.
- (6) Tranchemontagne, D. J.; Mendoza-Cortes, J. L.; O'Keeffe, M.; Yaghi, O. M. *Chem Soc Rev* **2009**, *38*, 1257.
- (7) Furukawa, H.; Ko, N.; Go, Y. B.; Aratani, N.; Choi, S. B.; Choi, E.; Yazaydin, A. O.; Snurr, R. Q.; O'Keeffe, M.; Kim, J.; Yaghi, O. M. *Science* **2010**, *329*, 424.
- (8) Li, J. R.; Kuppler, R. J.; Zhou, H. C. *Chem Soc Rev* **2009**, *38*, 1477.
- (9) Dinca, M.; Long, J. R. *J Am Chem Soc* **2005**, *127*, 9376.
- (10) Li, C. J.; Lin, Z. J.; Peng, M. X.; Leng, J. D.; Yang, M. M.; Tong, M. L. *Chem Commun* **2008**, 6348.
- (11) Navarro, J. A. R.; Barea, E.; Rodriguez-Dieguez, A.; Salas, J. M.; Ania, C. O.; Parra, J. B.; Masciocchi, N.; Galli, S.; Sironi, A. *J Am Chem Soc* **2008**, *130*, 3978.
- (12) Xue, M.; Ma, S. Q.; Jin, Z.; Schaffino, R. M.; Zhu, G. S.; Lobkovsky, E. B.; Qiu, S. L.; Chen, B. L. *Inorg Chem* **2008**, *47*, 6825.
- (13) Matsuda, R.; Kitaura, R.; Kitagawa, S.; Kubota, Y.; Belosludov, R. V.; Kobayashi, T. C.; Sakamoto, H.; Chiba, T.; Takata, M.; Kawazoe, Y.; Mita, Y. *Nature* **2005**, *436*, 238.

- (14) Lin, X.; Blake, A. J.; Wilson, C.; Sun, X. Z.; Champness, N. R.; George, M. W.; Hubberstey, P.; Mokaya, R.; Schroder, M. *J Am Chem Soc* **2006**, *128*, 10745.
- (15) Llewellyn, P. L.; Maurin, G.; Devic, T.; Loera-Serna, S.; Rosenbach, N.; Serre, C.; Bourrelly, S.; Horcajada, P.; Filinchuk, Y.; Ferey, G. *J Am Chem Soc* **2008**, *2008*, 12808.
- (16) Ferey, G.; Serre, C. *Chem Soc Rev* **2009**, *38*, 1380.
- (17) Greathouse, J.; Allendorf, M. D. *J Am Chem Soc* **2006**, *2006*, 10678.
- (18) Yaghi, A.; Li, H.; Eddaoudi, M. *J Am Chem Soc* **2000**, *122*, 1391.
- (19) Bourrelly, S.; Llewellyn, P. L.; Serre, C.; Millange, F.; Loiseau, T.; Ferey, G. *J Am Chem Soc* **2005**, 13519.
- (20) Kitaura, R.; Seki, K.; Akiyama, G.; Kitagawa, S. *Angewandte Chemie International Edition* **2003**, 428.
- (21) Murray, L. J.; Dinca, M.; Long, J. R. *Chem Soc Rev* **2009**, *38*, 1294.
- (22) van den Berg, A. W. C.; C., O. A. *Chem Commun* **2008**, 668.
- (23) Zaluska, A.; Zaluski, L.; Strom-Olsen, J. O. *Applied Physics A: Materials Science & Processing* **2001**, *72*, 157.
- (24) Kaye, S. S.; Dailly, A.; Yaghi, O. M.; Long, J. R. *J Am Chem Soc* **2007**, *129*, 14176.
- (25) Sun, Y. P.; Zhou, B.; Lin, Y.; Wang, W.; Fernando, K. A. S.; Pathak, P.; Meziani, M. J.; Harruff, B. A.; Wang, X.; Wang, H. F.; Luo, P. J. G.; Yang, H.; Kose, M. E.; Chen, B. L.; Veca, L. M.; Xie, S. Y. *J Am Chem Soc* **2006**, *128*, 7756.
- (26) Jensen, F. *Introduction to Computational Chemistry*; John Wiley & Sons Ltd: West Sussex, 2007.
- (27) Goddard, W. A.; Olafson, B. D.; Mayo, S. L. *J Phys Chem-US* **1990**, *94*, 8897.
- (28) Brooks, B. R.; III, C. L. B.; Jr, A. D. M.; Nilsson, L.; Petrella, R. J.; Roux, B.; Won, Y.; Archontis, G.; Bartels, C.; Boresch, S.; Caflisch, A.; Caves, L.; Cui, Q.; Dinner, A. R.; Feig, M.; Fischer, S.; Gao, J.; Hodoseck, M.; Im, W.; Kuczera, K.; Lazaridis, T.; Ma, J.; Ovchinnikov, V.; Paci, E.; Pastor, R. W.; Post, C. B.; Pu, J. Z.; Schaefer, M.; Tidor, B.; Venable, R. M.; Woodcock, H. L.; Wu, X.; Yang, W.; York, D. M.; Karplus, M. *Journal of Computational Chemistry* **2009**, *30*, 1545.

- (29) Rappe, A. K.; Casewit, C. J.; Colwell, K. S.; Goddard, W. A.; Skiff, W. M. *J Am Chem Soc* **1992**, *114*, 10024.
- (30) Smit, B.; Frenkel, D. *Understanding Molecular Simulation: From Algorithms to Applications*; Elsevier: San Diego, 2002.
- (31) Siepmann, I. J.; Martin, M. G. *J Phys Chem B* **1998**, *102*, 2569.
- (32) Garberoglio, G.; Skoulidas, A. I.; Johnson, J. K. *J Phys Chem B* **2005**, *2005*.
- (33) Maurin, G.; Ghoufi, A. *J Phys Chem C* **2010**, *114*, 6496.
- (34) Tan, J. C.; Cheetham, A. K. *Chem Soc Rev* **2011**, *40*, 1059.
- (35) Snurr, R.; Krishna, R.; Dubbeldam, D. *J Phys Chem C* **2009**, *113*, 19317.
- (36) S., C. D.; Cora, F.; Bell, R. G. *J Phys Chem C* **2009**, *113*, 544.
- (37) Salles, F.; Ghoufi, A.; Maurin, G.; Bell, R. G.; Mellot-Draznieks, C.; Férey, G. *Angewandte Chemie International Edition* **2008**, *47*, 8487.
- (38) Salles, F.; Ghoufi, A.; Maurin, G.; Bell, R. G.; Mellot-Draznieks, C.; Férey, G. *Angew Chem Int Ed Engl* **2008**, *47*, 8487.
- (39) Hamon, L.; Leclerc, H.; Ghoufi, A.; Oliviero, L.; Travert, A.; Lavalley, J.; Devic, T.; Serre, C.; Férey, G.; De Weireld, G.; Vimont, A.; Maurin, G. *J Phys Chem C* **2011**, *115*, 2047.
- (40) Cohen, S. M.; Wang, Z. *Journal of the American Chemical Society Communications* **2009**, *131*, 16675.
- (41) Karra, J. R.; Walton, K. S. *J Phys Chem C* **2010**, *114*, 15735.
- (42) Frisch, M. J. T., G. W.; Schlegel, H. B.; Scuseria, G. E.; Robb, M. A.; Cheeseman, J. R.; Scalmani, G.; Barone, V.; Mennucci, B.; Petersson, G. A.; Nakatsuji, H.; Caricato, M.; Li, X.; Hratchian, H. P.; Izmaylov, A. F.; Bloino, J.; Zheng, G.; Sonnenberg, J. L.; Hada, M.; Ehara, M.; Toyota, K.; Fukuda, R.; Hasegawa, J.; Ishida, M.; Nakajima, T.; Honda, Y.; Kitao, O.; Nakai, H.; Vreven, T.; Montgomery, Jr., J. A.; Peralta, J. E.; Ogliaro, F.; Bearpark, M.; Heyd, J. J.; Brothers, E.; Kudin, K. N.; Staroverov, V. N.; Kobayashi, R.; Normand, J.; Raghavachari, K.; Rendell, A.; Burant, J. C.; Iyengar, S. S.; Tomasi, J.; Cossi, M.; Rega, N.; Millam, N. J.; Klene, M.; Knox, J. E.; Cross, J. B.; Bakken, V.; Adamo, C.; Jaramillo, J.; Gomperts, R.; Stratmann, R. E.; Yazyev, O.; Austin, A. J.; Cammi, R.; Pomelli, C.; Ochterski, J. W.; Martin, R. L.;

Morokuma, K.; Zakrzewski, V. G.; Voth, G. A.; Salvador, P.; Dannenberg, J. J.; Dapprich, S.; Daniels, A. D.; Farkas, Ö.; Foresman, J. B.; Ortiz, J. V.; Cioslowski, J.; Fox, D. J.; Gaussian, Inc.: Wallingford, 2009.

(43) Wang, J.; Wang, W.; Kollman, P. A.; Case, D. A. *Molecular Graphics and Modelling* **2006**, *25*.

(44) Wang, J.; Wolf, R. M.; Caldwell, J. M.; Kollman, P. A.; Case, D. A. *Journal of Computational Chemistry* **2004**, *25*, 1157.

(45) Case, D. A.; Darden, T. A.; Cheatham, T. E.; Simmerling, C. L.; Wang, J.; Duke, R. E.; Luo, R.; Walker, R. C.; Zhang, W.; Merz, K. M.; Roberts, B.; Wang, B.; Hayik, S.; Roitberg, A.; Seabra, G.; Kolossvai, I.; Wong, K. F.; Paesani, F.; Vanicek, J.; Liu, J.; Wu, X.; Brozell, S. R.; Steinbrecher, T.; Gohlke, H.; Cai, Q.; Ye, X.; Wang, J.; Hsieh, M. J.; Cui, G.; Roe, D. R.; Mathews, D. H.; Seetin, M. G.; Sagui, C.; Babin, V.; Luchko, T.; Gusarov, S.; Kovalenko, A.; Kollman, P. A. 2010.

(46) Todorov, I. T.; Smith, W. 2010.

(47) Dybtsev, D. N.; Chun, H.; Kim, K. *Angew Chem Int Edit* **2004**, *43*, 5033.

(48) Lee, J. Y.; Olson, D. H.; Pan, L.; Emge, T. J.; Li, J. *Adv Funct Mater* **2007**, *17*, 1255.

(49) Lee, J. Y.; Olson, D. H.; Pan, L.; Emge, T. J.; Li, J. *Adv Funct Mater* **2007**, *17*, 1255.

(50) Chun, H.; Dybtsev, D. N.; Kim, H.; Kim, K. *Chemistry* **2005**, *11*, 3521.

(51) Uemura, K.; Yamasaki, Y.; Komagawa, Y.; Tanaka, K.; Kita, H. *Angew Chem Int Ed Engl* **2007**, *46*, 6662.

(52) Chen, Z. X.; Xiang, S. C.; Zhao, D. Y.; Chen, B. L. *Cryst Growth Des* **2009**, *9*, 5293.

(53) Chen, Y. F.; Lee, J. Y.; Babarao, R.; Li, J.; Jiang, J. W. *J Phys Chem C* **2010**, *114*, 6602.

(54) Liang, Z. J.; Marshall, M.; Chaffee, A. L. *Micropor Mesopor Mat* **2010**, *132*, 305.

(55) Lee, E.; Kim, J. K.; Lee, M. *Angew Chem Int Edit* **2009**, *48*, 3657.

(56) Liang, Z.; Marshall, M.; Chaffee, A. L. *Micropor Mesopor Mat* **2010**, *132*, 305.

- (57) Snurr, R.; Ellis, D.; Walton, K. S.; Galvin, C.; Dubbeldam, D. *J Am Chem Soc* **2008**, 10884.
- (58) Feynman, R. P. *Statistical Mechanics; A Set of Lectures*; W. A. Benjamin: Reading: MA, 1972.
- (59) Feynman, R. P.; Hibbs, A. R. *Quantum Mechanics and Path Integrals*; McGraw-Hill: New York, 1965.
- (60) Walton, K. S.; Karra, J. R. *J Phys Chem C* **2010**, 15735.
- (61) Jiang, J. W.; Babarao, R.; Lee, J.; Chen, Y. B. *J Phys Chem C* **2010**, 6602.
- (62) Cramer, C. J. *Essentials of Computational Chemistry - Theories and Models*; John Wiley & Sons Inc.: New Jersey, 2009.
- (63) Stephens, P. J.; J, D. F.; Chabalaowski, C. F.; Frisch, M. J. *J Phys Chem-Us* **1994**, 98, 11623.
- (64) Liu, B.; McLean, A. D. *J Chem Phys* **1973**, 59, 4557.
- (65) Cox, S. R.; Williams, D. E. *Journal of Computational Chemistry* **1981**, 2, 304.
- (66) Kollman, P. A.; Singh, U. C. *Journal of Computational Chemistry* **1983**, 5, 129.
- (67) Besler, B. H. *Journal of Computational Chemistry* **1989**, 11, 431.
- (68) Bayly, C. I.; Cieplak, P.; Cornell, W. D.; Kollman, P. A. *J Phys Chem-Us* **1993**, 97, 10269.
- (69) Chirlian, L. E.; Francl, M. M. *Journal of Computational Chemistry* **1987**, 8, 894.
- (70) Breneman, C. M.; Wiberg, K. B. *Journal of Computational Chemistry* **1990**, 11, 361.
- (71) Francl, M. M.; Carey, C.; Chirlian, L. E.; Gange, D. M. *Journal of Computational Chemistry* **1996**, 17, 367.
- (72) Dunning, T. H. *J Phys Chem-Us* **1989**, 90, 1007.
- (73) Dunning, T. H.; Woon, D. E. *J Chem Phys* **1993**, 98, 1358.

- (74) Tafipolsky, M.; Amirjalayer, S.; Schmid, R. *Micropor Mesopor Mat* **2010**, *129*, 304.
- (75) Zhao, Y.; Truhlar, D. G. *Theoretical Chemistry Accounts: Theory, Computation, and Modeling* **2008**, *120*, 215.
- (76) Chen, Z.; Xiang, S.; Zhao, D.; Chen, B. *Cryst Growth Des* **2009**, *9*, 5293.
- (77) Schmid, R.; Amirjalayer, S.; Tafipolsky, M. *J Phys Chem C* **2010**, *2010*, 14402.